Spectroscopic Studies of Excited Species Reflected from Solid Surfaces Irradiated by DC Plasma Cathode Systems

JHOELLE ROCHE MENDIOLA GUHIT

A dissertation submitted in partial fulfilment
of the requirements for the degree of
Doctor of Engineering

The Graduate School of Science and Engineering
Department of Electrical and Electronic Engineering
Doshisha University

Kyoto, Japan
2020

Synopsis

In this study, the author studied the Excited Species Reflected from Solid Surfaces Irradiated by DC Plasma Cathode Systems through spectroscopic investigation. The author also develops a new duoplasmatron ion source that can be used as a plasma cathode and positive ion source. The author employed the technique to investigate the excited states particle reflected using Doppler spectroscopy previously developed for detecting hydrogen Balmer emissions.

Doppler-broadening of the Hα emission spectra from hydrogen reflected at surfaces of palladium and tungsten sheet metal surfaces held at clamp holders were presented in this study. The reflected hydrogen atoms were observed with velocity components produced by the back scatterings of H_3^+ H_2^+ and H^+ ion incident regions. Palladium exhibited higher spectrum emission intensities than tungsten for both clamp structures. Modification of the clamp structure should produce cooler surface condition due to direct contact of metal surface to the substrate holder thus having H atoms adsorbed more on the palladium sheet.

Hydrogen plasma-metal surface interactions accompany molecular excitations and de-excitations associated with particle reflection at the surfaces. Optical light emissions from molecular species of the hydrogen Fulcher-α $(d^3\Pi_u^- \rightarrow a^3\Sigma_g^+)$ Q-Branch at near metal surface region of palladium and tungsten metals were investigated. A wide wavelength range spectrometer indicated a higher emission spectrum of hydrogen plasma on the surface of palladium than tungsten. Meanwhile a high-resolution spectrometer showed the distinct rovibronic lines of the Fulcher-α for electronic levels $v = v' = 0 - 4$ transitions. Rotational temperature, T_{rot}, were computed from the emission spectra lines of hydrogen from palladium and tungsten surfaces. The obtained temperature, T_{rot} for both metal targets showed increase at increasing negative bias voltages applied onto the target of these

materials. Hydrogen plasma on palladium surface indicated higher molecular excitations than that on the tungsten surface.

For duoplasmatron plasma cathode, a 280 G linear magnetic field sustained a 2.5 mm diameter stable hydrogen plasma column produced by a duoplasmatron plasma cathode. A high-intensity magnetic field created by a pair of permanent magnets and the field compression structure realized the passage of a dense plasma flow through a 2 mm diameter hole. Both ions and electrons can be extracted from the downstream plasma where a linear magnetic field can be induced to guide the plasma for striking a tungsten target. Luminous intensity distribution around a tungsten target located at another end of the magnetic field confronting to the plasma cathode was examined. A substantial reduction in the Hα line spectral broadening was observed that enabled a precise spectroscopic study of the hydrogen particle reflection at the solid target surface.

Acknowledgments

Lastly, to God. I know that I have not been going to church, but I do believe in you. I do believe in your existence and power. I know that throughout these years, that you have been taking care of me, my family, and friends. I thank you for the blessings that you have bestowed on me.

Contents

List of Figures

List of Tables

Chapter 1   Introduction

1.1   Plasma-Wall Interaction

The Figure 1.1 shows the cross-section of ITER (originally known as the International Thermonuclear Experimental Reactor) (Samm, 2006). Atomic and Molecular Physics, Chemistry, Material Science, Surface Physics: These subjects can be combined into a bigger field and utilized in the field of plasma-wall interaction. One major area wherein plasma-wall interaction is heavily studied are inside fusion devices like this figure. The inner region of the fusion device is exposed directly to the plasma process. (Linke, 2019)

The divertor region is of interest since these functions as removal of waste material from the plasma while the reactor is still operating. This then exposes the region's surface to the plasma and its impurities which can cause multiple plasma surface reactions like melting, sputtering, and sublimation. Therefore, selecting the type of material to create the divertor region parts and inner walls of the fusion devices is highly significant. (Thomser, 2012)

Figure 1.2– Combination of wall materials for plasma-loaded surfaces in ITER (Samm, 2006) depicts the possible wall combination of wall materials for plasma-loaded surfaces in ITER which composed of a combination of different materials: Beryllium (Be), Graphite (C), and tungsten (W). The possible combination of these materials fulfills the requirements with their specific characteristics for very different loads at different wall

areas. Generally, the local and global plasma processes lead to a strong reduction of net erosion – like the divertors or limiters. Indeed, materials to be used inside the chambers are very important to have less corrosion and low sputtering yield. (Linke, 2019)
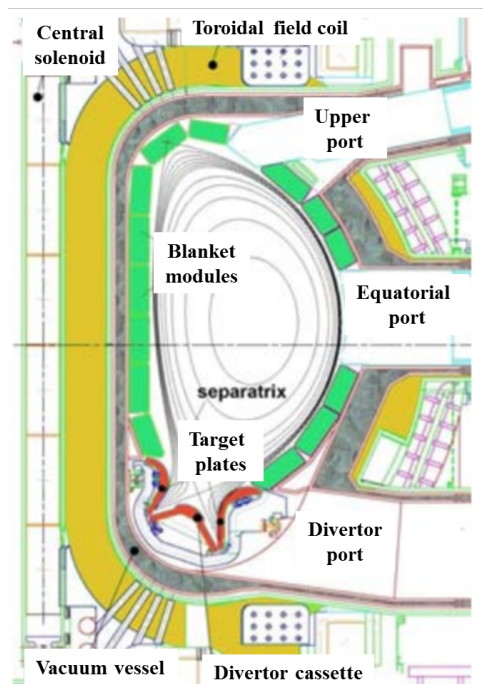
Figure 1.1– Cross section of ITER (International Thermonuclear Experimental Reactor)
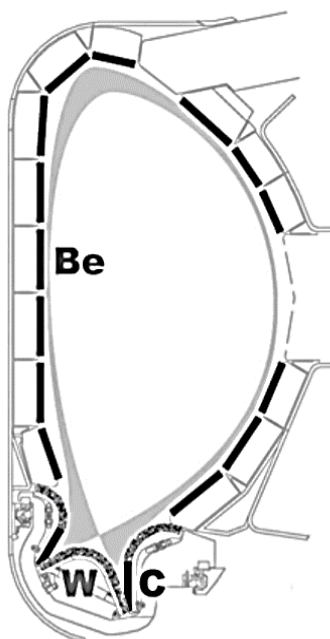
Figure 1.2– Combination of wall materials for plasma-loaded surfaces in ITER

1.2 Scope of the Study

Hydrogen plasma interaction on metal wall surfaces causes surface permeation or erosion and plasma impurity emission in which investigating and analyzing these phenomena are significant in the advancement of fusion research and device development. The phenomena must be studied before fusion devices will be put into operation with the long life-time. It is consequently of interest to examine and understand the underlying mechanisms of hydrogen isotope permeation and particle release during plasma-surface interactions. Permeation of hydrogen through metallic materials like palladium is of vital concern to control transport and mass separation of hydrogen isotopes in the system. Palladium (Pd), in comparison to tungsten (W), has a strong absorbance of hydrogen molecules and can show unique behavior in a hydrogen plasma environment due to the nature of rapid hydrogen isotope transport. Thus, a comparative study in hydrogen reflection between Pd and W has been made using a small plasma exposure device.

In addition, atomic and molecular processes in low pressure plasmas are examined in fusion edge plasmas. Both atoms and molecules can be excited through collisions in the plasma region. Molecular excitation is more complicated due to the additional quantum numbers, v and j, for both vibrational and rotational (rovibrational) quantum numbers, respectively. These values can identify rotational (T_{rot}) and vibrational (T_{vib}) temperatures to understand the underlying phenomena in the molecular and atomic excitations. Hydrogen forms a diatomic molecule in a room temperature laboratory

condition and this paper limits the investigation to T_{rot}. The temperature T_{rot} can be derived through examining and identifying the rovibronic emission lines from the hydrogen Fulcher-α bands (Shikama, 2007). In this paper, emission spectroscopy identifies the rovibronic lines of the hydrogen Fulcher-α $(d^3\Pi_u^- \rightarrow a^3\Sigma_g^+)$ Q -Branch at the near metal surfaces of palladium and tungsten targets immersed in hydrogen plasma.

Furthermore, fundamental processes in plasma material interactions are often investigated using a linear device with an electron emission cathode for quasi-steady-state operations. A small device driven by a high-temperature tungsten cathode was developed to study Hα line spectrum profiles that are Doppler-broadened due to particle reflection at a metal surface in a hydrogen plasma . The line of sight for the measurement was set outside of the plasma to reduce noise due to photon emissions from the plasma. The measured spectra showed clear broadening corresponding to the velocity distributions of reflected particles when their incident energies were higher than 200 eV. The observed spectrum showed a substantial broadening that could not be explained by the particle reflection at the target; the spectrum showed broadening at the skirt part even at low (less than 150 eV) hydrogen ion bombardment energy. The large plasma radius and the exposed target area may cause the velocity and the angular distributions of both incident and reflected hydrogen particle to vary and thus can enlarge the broadening of the Hα line spectrum. Meanwhile, a smaller diameter plasma is preferred because the line of sight for the spectroscopic measurement should be set as close to the particle emission point as possible. A duoplasmatron source can produce intense plasma that can pass through an aperture less than 0.13 mm diameter. This small size plasma ball can produce both ions and electrons depending upon the extraction voltage. In this report, we couple a small duoplasmatron

source to a linear magnetic field to sustain small diameter plasma. Plasma termination and instability is also discussed.

The succeeding chapter, Chapter 2, discusses some principles for plasma surface interaction. Chapter 3 discusses the methodology and the two DC plasma cathode systems used in this study. Chapter 4 shows the Doppler broadening mechanisms of hydrogen and helium plasma on different metal surfaces coupled with ACAT simulations. Chapter 5 discusses the spectroscopic investigation to study the rotational transition of hydrogen plasma on tungsten and palladium surfaces. Chapter 6 examines and demonstrates the newly assembled duoplasmatron ion source. Chapter 7 summarizes the whole study provides the conclusion.

References

Linke, J., Du, J., Loewenhoff, T., Pintsuk, G., Spilker, B., Steudel, I., & Wirtz, M. (2019). Challenges for plasma-facing components in nuclear fusion. Matter And Radiation At Extremes, 4(5), 056201. doi: 10.1063/1.5090100

Samm, U. (2006). Plasma-Wall Interaction. *Fusion Science And Technology*, *49*(2T), 234-239. doi: 10.13182/fst06-a1122

SHIKAMA, T., KADO, S., KUWAHARA, Y., KURIHARA, K., SCOTTI, F., & TANAKA, S. (2007). Fulcher-α Band Spectra in Mixed Hydrogen Isotope Plasmas. Plasma And Fusion Research, 2, S1045-S1045. doi: 10.1585/pfr.2.s1045

Thomser, C. (2012). Plasma Facing Materials for the JET ITER-Like Wall. *Fusion Science & Technology*. doi: 10.13182/fst11-454

Zheng, L., Kotschenreuther, M., & Van Dam, J. (2009). Kinetic analysis of the resistive wall modes in the ITER advanced tokamak scenario. *Nuclear Fusion*, *49*(7), 075021. doi: 10.1088/0029-5515/49/7/075021

Chapter 2   Principles

2.1   Plasma-Surface Interaction

The interaction between surfaces of materials and plasma bombardment is called Plasma Surface Interaction (PSI). As research progress throughout the years, different concepts and studies have arisen and experiments were conducted. ITER or the International Thermonuclear Experimental Reactor, is one of the famous research facilities in France which support the studies on PSI. Surfaces that being studied are called plasma facing materials and interaction with the plasma is being supported on both theoretical and experimental research to understand the phenomena behind it. Plasma-surface interactions can be diverse, and include for example, the emission of secondary electrons from a surface due to electron, ion, neutral, or radiation bombardment, the removal of atoms from surfaces due to sputter erosion, deposition of thin films, and charging of surfaces by electrons or ions.

Figure 2.1– Plasma-surface physical interaction (Binder, 2013) is being shown. Once the plasma bombards the surface interface, certain phenomena exist as the ions interacts with the material. Presence of reflected ions and neutral species is observed as well as secondary electrons. Sputtering and even heating of surface can also occur due to the high temperature properties of the plasma on the surface. In addition, bulk penetration can also occur in the form of structural rearrangement due to electrons penetrating the surface. Ion implantation can also occur depending on plasma conditions and parameters. In DC glow discharges type of plasma source, depending

on the electrode configuration and how the samples or parts are placed in the plasma chamber, the influence of the plasma species bombardment will be more or less important.
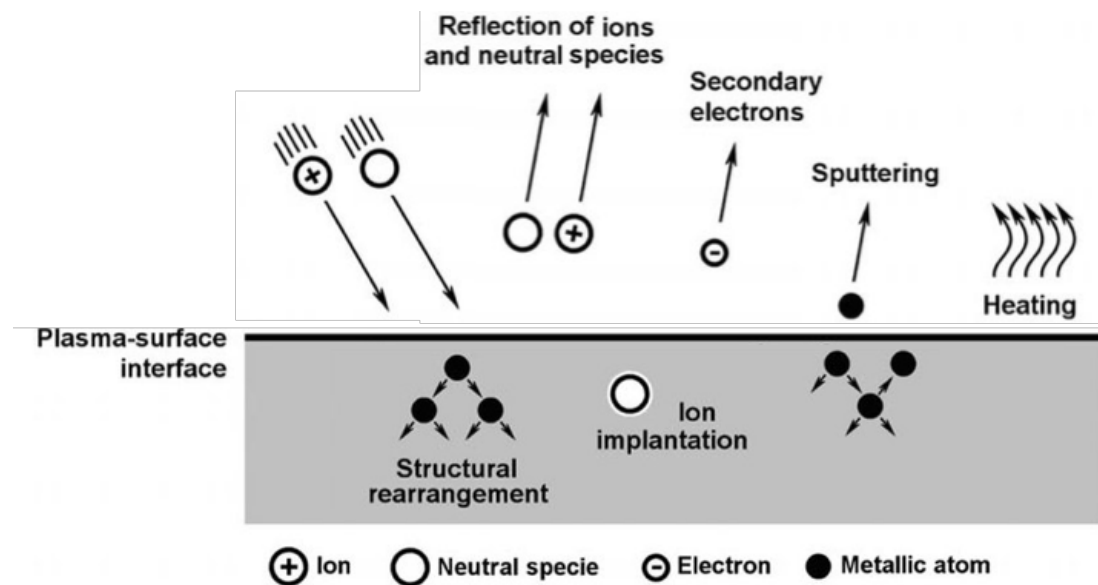
Figure 2.1– Plasma-surface physical interaction (Binder, 2013)

2.2 Plasma Sheath Formation

A fundamental concept in the plasma-surface interaction is the formation of a plasma sheath on the region on the material surface contact. This sheath comprises of the plasma species, its reaction on the material surface, and the resulting ions due to this interaction hence it's called the plasma sheath region. This can also result to etching when the there is a difference between the sheath and plasma region's potential. A schematic diagram for this plasma sheath can be seen in Figure 2.2– Plasma Sheath (Mesko, 2005). This depicts that when the positive ions and electrons are of a certain distance from the surface, the potential density of the bulk plasma is much higher. It is also seen that $n_e \approx n_i =$

n where this describes that the current densities of both electrons and ions are almost the same. A region wherein the potential density starts to decrease, and that electron loss is being observed. Thus, the region will form neutrals and positive ions which in turns accelerates to the boundary region. This region has the negative region lower tremendously wherein electrons can be pushed away or expelled from the sheath region thereby having loss of electron density. This region also not glow as much due to electron impact excitation reduction sometimes called the dark space. (Wang, 2019)
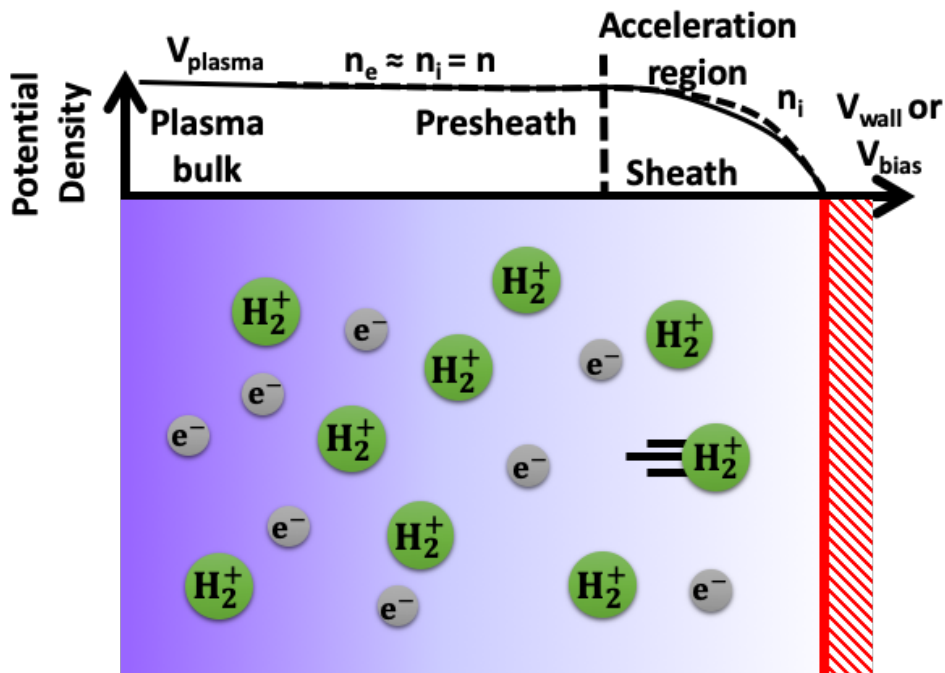
Figure 2.2– Plasma Sheath (Mesko, 2005)

2.3   Hydrogen and Balmer Series

Research on the plasma-surface interaction led to the usage of the different gasses and materials and the leading gasses used is hydrogen. Hydrogen studies on surfaces, especially tungsten, lead to different studies on spectral line emissions. One further observed in this study is the Balmer series base from the Balmer lines to describe such phenomenon in the visible spectrum. (Lafleur, 2019)

This spectrum line is composed of four distinct wavelengths: 410 nm, 434 nm, 486 nm, and 656 nm. These wavelengths correspond to the different level of emission of a photon depending on their quantum energy level and can be observed as depicted in Figure 2.3– Rutherford Bohr model of the hydrogen atom. (Dieke, 1958)
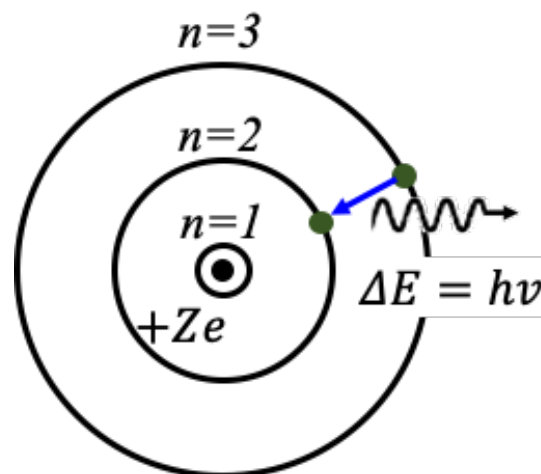
Figure 2.3– Rutherford Bohr model of the hydrogen atom

From the figure, different energy levels show the electron transitions and that the Balmer series corresponds to the following: $n \geq 3$ to $n = 2$. The n value level here is the principal or radial quantum number of the hydrogen electron. Different Greek letter

represents these transitions: H_α: n level 3→2, H_β: n level 4→2, H_γ: n level 5→2, and H_δ: n level 6→2. The first three Greek letters correspond are of interest since this is observed in the visible part of the electromagnetic spectrum. Figure 2.4– Optical emission spectroscopy of hydrogen plasma on tungsten surface and corresponding Balmer series transition is depicted.

The H_α spectrum peak emission have the highest intensity due to the energy level closest to the n=2 level. This corresponds to 656.28 nm in the visible range. The second is H_β and corresponds to the second highest peak since this is next energy level n=4 and have the 486.13 nm wavelength. The third, H_γ, have the wavelength of 434.05 nm. These three indicates the atomic conditions of the plasma. A fourth region called the Fulcher-α region is studied to understand the molecular of the hydrogen plasma. (Dieke, 1958)
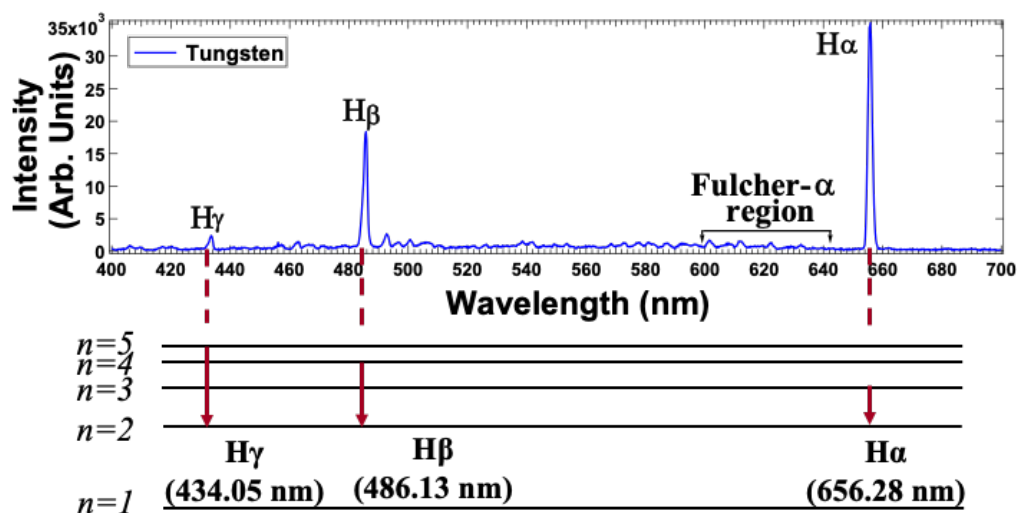
Figure 2.4– Optical emission spectroscopy of hydrogen plasma on tungsten surface and corresponding Balmer series transition

2.4 Helium Atom
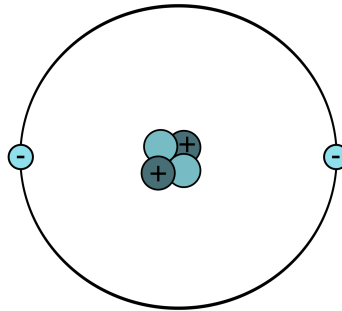
Figure 2.5– Helium Atom
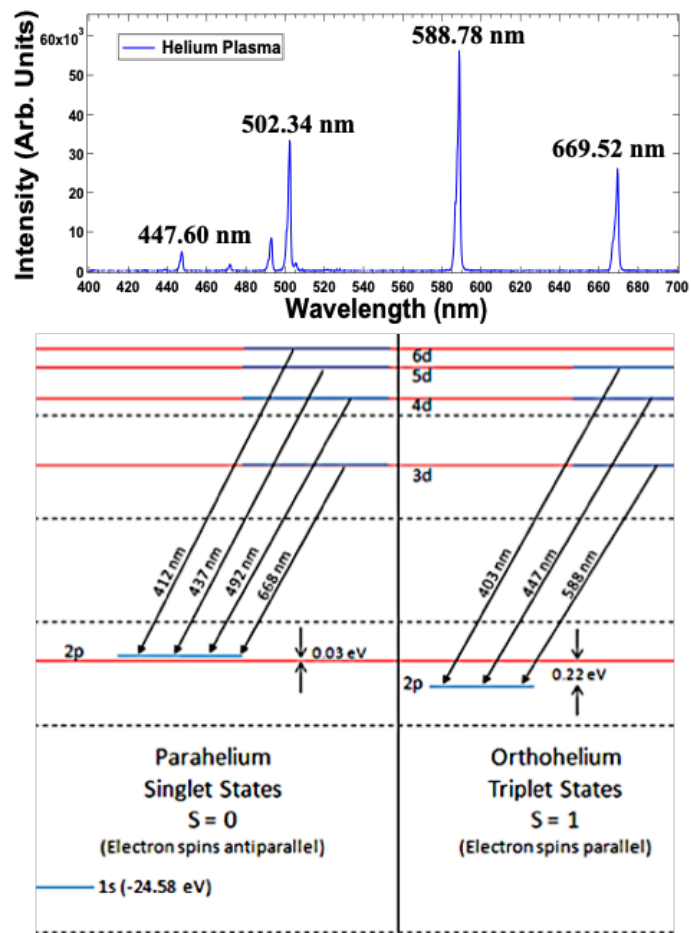
Figure 2.6– Optical emission spectroscopy of helium plasma on tungsten surface and

corresponding transition (Ahn, 2007)

The difference in transition is shown in Figure 2.6– Optical emission spectroscopy of helium plasma on tungsten surface and corresponding transition (Ahn, 2007). It shows that depending on the electron spin, either parallel or antiparallel, it corresponds to the parahelium (singlet) or orthohelium (triplet). My official helium spectrum is shown on top of this figure. Please see Figure 4.12– Helium spectra in the visible range for further explanation on the wavelengths that corresponds to the singlet and triplet state and its relation to the Doppler broadening.

References

Ahn, J.-W., Craig, D., Fiksel, G., Den Hartog, D. J., Anderson, J. K., & O'Mullane, M. G. (2007). Emission intensities and line ratios from a fast neutral helium beam. *Physics of Plasmas*, *14*(8), 083301. https://doi.org/10.1063/1.2759191

Dieke, G. (1958). The molecular spectrum of hydrogen and its isotopes. Journal Of Molecular Spectroscopy, 2(1-6), 494-517. doi: 10.1016/0022-2852(58)90095-x

Lafleur, T., Schulze, J., & Donkó, Z. (2019). Plasma-surface interactions. Plasma Sources Science And Technology, 28(4), 040201. doi: 10.1088/1361-6595/ab1380

Wang, X., Robertson, S., & Horányi, M. (2019). Plasma Sheath Formation at Craters on Airless Bodies. *Journal Of Geophysical Research: Space Physics*, *124*(6), 4188-4193. doi: 10.1029/2018ja026235

Chapter 3   DC Plasma Cathode System

The actual setup of the DC plasma cathode device is in Figure 3.1– Actual DC Plasma Cathode Device. We have three main areas: The power supply rack wherein we placed all auxiliary voltage sources, the hydrogen generator and vacuum pump controller; The center portion is the DC Plasma Cathode System is composed of the main chamber and the vacuum system; and the third area is where a set of mirrors projects the plasma towards the monochromator spectrometer with 23 pm resolution.
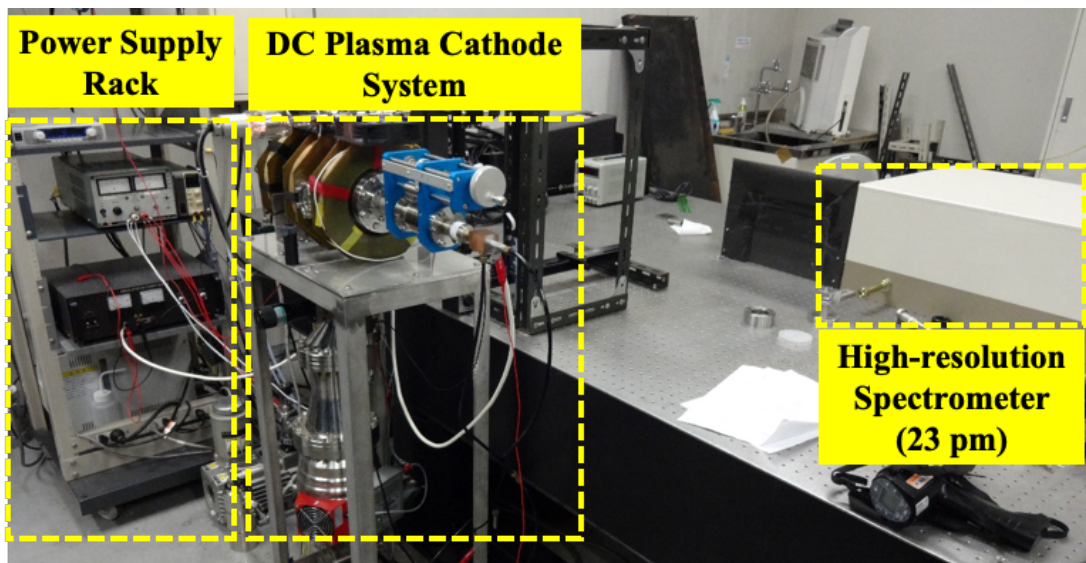
Figure 3.1– Actual DC Plasma Cathode Device

3.1   Schematic Diagram

Figure 3.2 shows the schematic diagram of the DC plasma cathode device. One of the previous methods develop in this device is the measurement to determine the doppler

broadening of the reflected atoms by detecting the collisions occur outside the plasma vicinity. These collisions occur perpendicular to the 45-degree angle position of the target holder (Doi, 2018).

The external parts of the device are as follows: We have the electrode feedthrough to provide current to the filament; three external electromagnetic coil which produces a magnetic field intensity of 280 G; a manipulator to adjust the distance of the holder from the center view port; the target bias power supply source; and the embedded circuit diagram for electron extraction. An ICF70 viewport flange to check for alignment and reflection measurement is positioned at the center of the chamber.
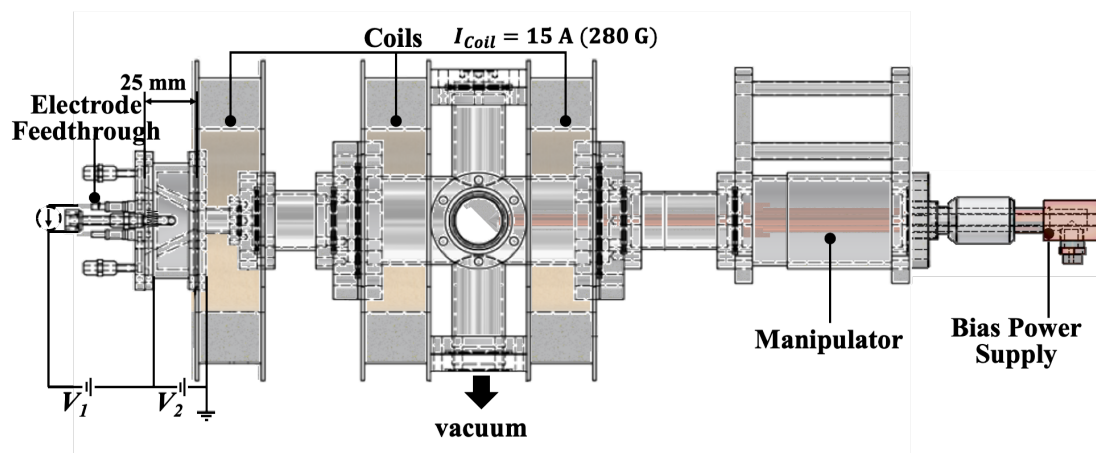
Figure 3.2– Schematic diagram of the DC plasma cathode device

In Figure 3.3 shows the DC plasma cathode device cross-section which illustrates a detailed schematic diagram of Figure 3.1. This apparatus irradiated tantalum (Ta) palladium (Pd) and tungsten (W) metal sheets by a linear magnetized hydrogen plasma.

These metal materials are 0.1 mm thick, 24 mm wide and 25 mm long in size. An 18.7 mT magnetic field is produced by three pancake coils. Each coil current input is 5 A and connected in parallel around the device to create linear magnetic-force lines that extended the electrons from the tungsten filament cathode to the target substrate holder. Starting at the left most portion of the figure, the tungsten filament wire connected to the electrode feedthrough for the thermionic emission of ionizing electrons.

The embedded circuit diagram for the filament region indicates two DC power supplies, in series connection. Both power supplies are maintained with discharge current of I_2 = 1.0 A and 70 V for both V_1 and V_2 for applied potentials. These are used to extract electrons from the filament and generate the hydrogen gas discharge. Hydrogen gas pressure is set at 1.2 Pascal. When using helium gas, the pressure is at 0.2 Pa. These conditions generate a hydrogen or helium cylindrical-shaped magnetized plasma with a diameter is 15 mm. A viewing port of BK7 (borosolicate glass) is fitted with an ICF70 flange for the alignment of the substrate holder and hydrogen reflection measurement.

The plasma beam interacts with the target metal surface attached to the holder where a backside water cooling gas is attached. The target surface is attached to a substrate holder angled at a 45-degrees parallel to plasma. Usual electron density ranges around 10^{11} cm^{-3} and with electron temperature of a few eV. A viewport is positioned parallel to the plasma to observe emission spectra lines outside the vicinity of the beam. Negative bias voltages were applied to the substrate holder starting from -100 V at an increment of -100 V to -600 V maximum through a DC power supply.

The -600 V is the maximum limit for the current device configuration. Nevertheless, this was maximized through a modified clamp discussed in Chapter 4.2. The molecular and atomic spectra at the vicinity of the bombarded metal sheets of Pd and W were observed through a 0.23 Å wavelength resolution Czerny-turner monochromator. The wavelength used for Hα observation was set around 656.28 nm to monitor the atomic emissions. A continuously cooled CCD detector, S7034-1007S of Hamamatsu Photonics, with 60 seconds integration time recorded the output spectra.
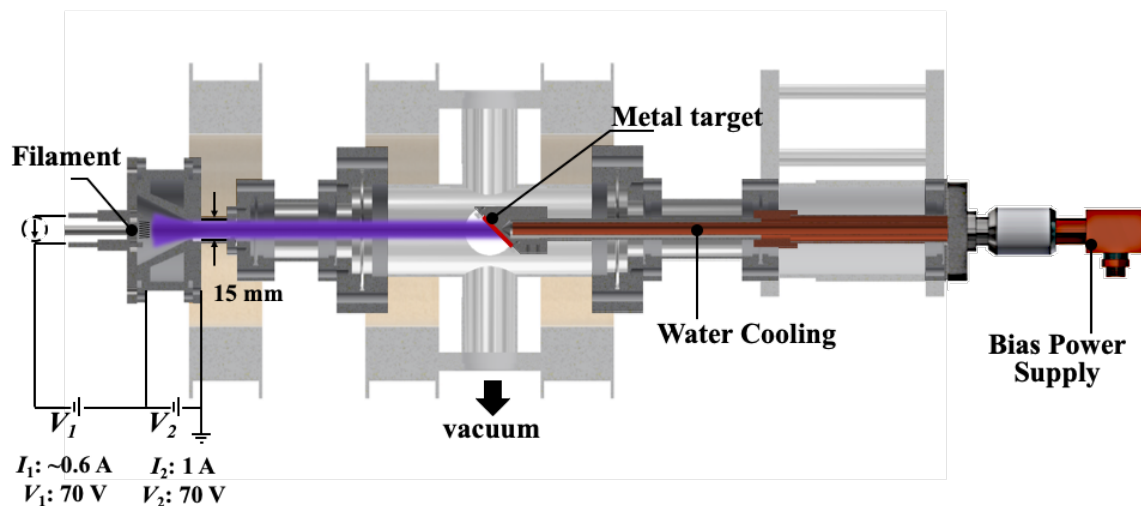
Figure 3.3–DC plasma cathode device cross section

A continuous water flow at the backside of the holder was maintained to avoid excessive heating of the target, as temperature exceeded 1100 K during a hydrogen plasma bombardment onto the target maintained (Doi, 2018). Meanwhile, the surface temperature of the target mounted by the modified clamp cannot be evaluated as the temperature was below 800 K, which was the detection limit for the infrared radiation thermometer.

3.2   Plasma-Surface Interaction on Metal Target
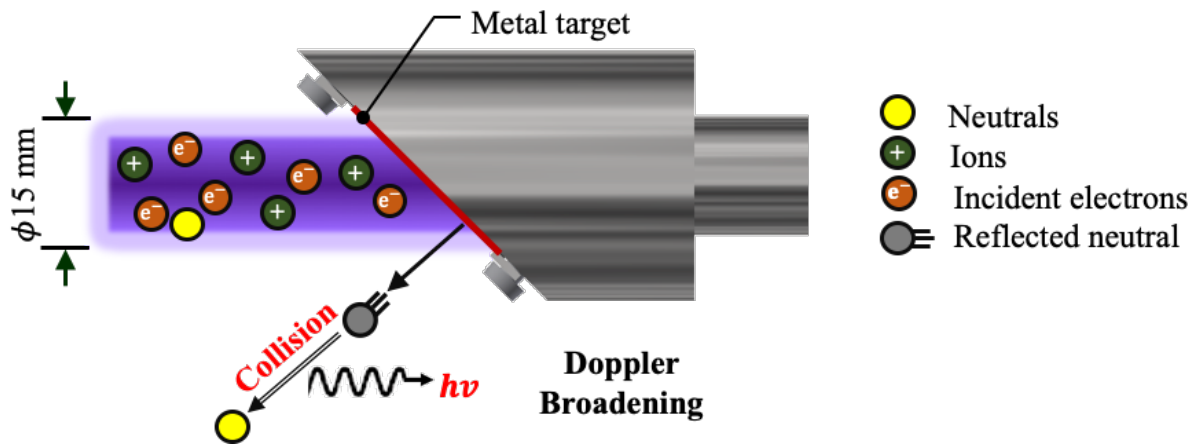
Figure 3.4–DC plasma cathode device cross section

Figure 3.4 is a detailed view of the target holder that shows the particle reflection on metal targets inside the chamber, compose of neutrals/ions/electrons. Once these hits (and the target is negatively biased) the positive ions approached the surface while the neutrals are reflected perpendicular to the target. This neutral is much energetic due to reflection collision. When this collides with nearby neutral, this collision releases hv. A profile is measured through the spectrometer to obtain the spectral profile.

The broadening of spectral profile lines due to the Doppler effect caused by a distribution of velocities of atoms or molecules is called the Doppler broadening. Different velocities of the emitting particles result in different Doppler shifts, the cumulative effect of which is the line broadening. This resulting line profile is known as a Doppler profile. The spectroscopic measurement method of the Doppler broadening is shown Figure 3.5.

This method previously developed to obtain the Doppler broadening from the 45-degree angled target holder (Doi, 2018). The location of interest to obtain the profile is outside of the plasma vicinity. But perpendicular to the target. The observation of interest to detect and investigate the Doppler-broadening due to the velocity distribution of hydrogen reflection at the tungsten and palladium metal sheets.
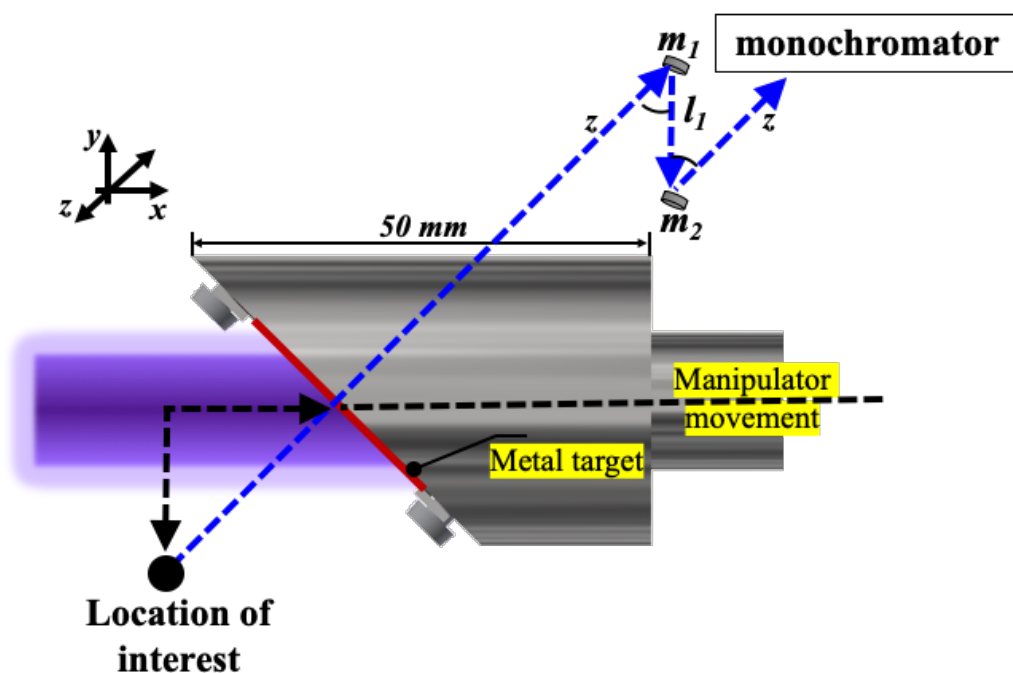
Figure 3.5–Spectroscopic measurement of Doppler broadening

By setting the line of sight outside of the plasma column, all lines emissions from molecules directly excited by plasma electrons are excluded in the spectrum (Doi, 2018). To be able to obtain the proper location of interest, we use the manipulator to move the target to the right and away from the center. The first mirror, m_1, is perpendicular through the z-axis of the spot. It is moveable at the y-axis direction where $l_1 = 9$ mm. A second

mirror, m_2, is placed below and not moveable. Both m_1 and m_2 are angled at 45 degrees. The light from the plasma is guided to the monochromator through m_1 and m_2 mirrors outside the chamber. The adjustments on the manipulator and positioning of m_1 are made to observe the emission spectra outside the plasma boundary. This mirror is set to observe perpendicularly the area of interest.
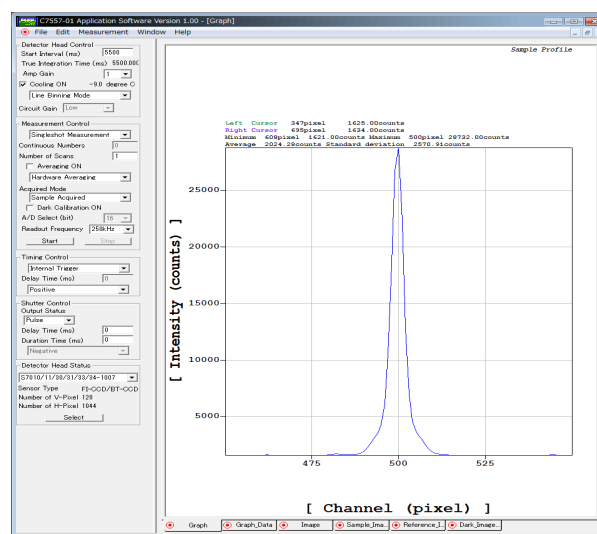
Figure 3.6–Typical spectral profile from the monochromator

Figure 3.6 is the typical spectral profile obtained from the monochromator. This monochromator spectrometer has a high resolution of 23 picometer to identify these profile broadening and the system can adjust the wavelength, within visible range, to select a specific wavelength to observe the transitions. For each profile, the regions of the reflected ions can be separated by region in the spectra from the general equation of wavelength shift, $\Delta\lambda$, calculated by the following equation (3.1).

$$\Delta\lambda = \frac{\lambda_a}{c}\sqrt{\frac{2eE_b}{M}} \qquad (3.1)$$

Here, λ_α is the wavelength of H_α or 656.28 nm, e is the charge of the electron, E_b is the bias voltage at -600 V or 600 electron volts, M is the mass of the ion to be investigated and c is the speed of light. This equation determines the regions where contributions from which ions are present. The fast electronically excited hydrogen atoms manifest themselves in broadened wings of the spectral lines in a plasma emission.

3.3 ACAT Simulation

Figure 3.7–ACAT Simulation method concept

24
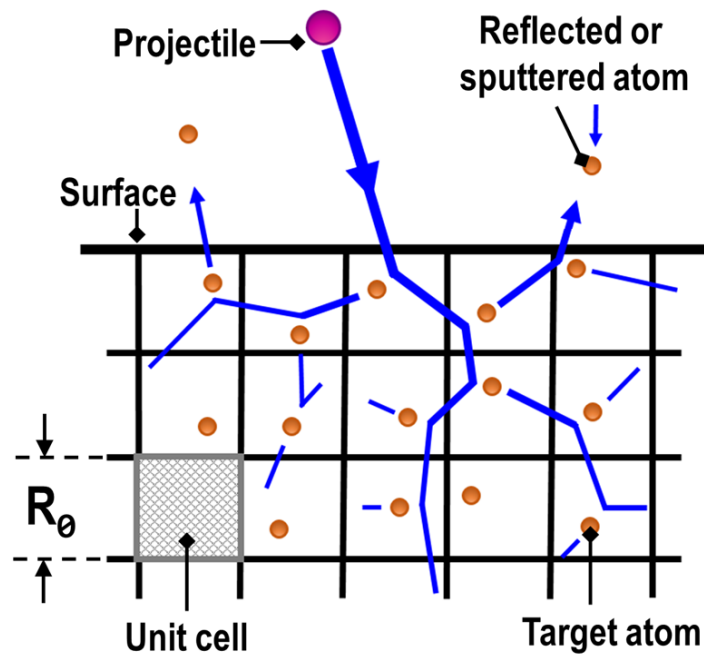
Figure 3.7–ACAT Simulation method concept shows how the projected particle
surface interacts on the wall surface. Shows that some particles are reflected, and some are
absorbed at the surface.

The collision process of atoms, computed from the binary collision approximation
and Monte Carlo Method, is simulated using the A Atomic Collision Amorphous Target
system or simply ACAT code (Kenmotsu, 2021). All the conditions base from Figure 3.7–
ACAT Simulation method concept uses the assumption of a two-body system under the
binary collision approximations. This code has been utilized for other surfaces like cesium,
carbon nanowalls, molybdenum, tungsten. (Tanaka, 2009) ACAT code can be utilized with
applied target bias of >100 V. This is used to predict the Doppler broadening of reflected
hydrogen and helium atoms on tungsten, palladium, and tantalum surfaces. (Kato, 2015)

References

Doi, K., Lee, H. T., Tanaka, N., Yamaoka, H., Ueda, Y., & Wada, M. (2018). Spectroscopic study of hydrogen reflection at modified tungsten surface. *Fusion Engineering and Design, 136*, 100-105. doi:10.1016/j.fusengdes.2018.01.001

Kato, S., Tanaka, N., Sasao, M., Kisaki, M., Tsumori, K., Nishiura, M., . . . Yamaoka, H. (2015). Angle-resolved intensity and energy distributions of positive and negative hydrogen ions released from tungsten surface by molecular hydrogen ion impact. *Journal of Nuclear Materials, 463*, 351-354. doi:10.1016/j.jnucmat.2014.12.026

Kenmotsu, T., & Wada, M. (2012). Effects of adsorption and roughness upon the collision processes at the convertor surface of a plasma sputter negative ion source. *Review of Scientific Instruments, 83*(2). doi:10.1063/1.3673624

Tanaka, N., Yamaoka, H., Nishiura, M., Tsumori, K., Nagamura, T., Sasao, M., . . . Wada, M. (2009). Low-energy particle interaction at carbon nanowalls on W surface. *Journal of Nuclear Materials, 390-391*, 1035-1038. doi:10.1016/j.jnucmat.2009.01.281

Chapter 4　Doppler Broadening of Reflected Atoms on Metal Surfaces

We focus on H-alpha since this is the transition with the highest intensity as previously mπmentioned of the hydrogen emission spectrum. We are interested in velocity distributions of reflected atoms from the surface of the metal targets and obtain the Doppler profile broadening and compare it to ACAT code. We will use hydrogen plasma on tungsten, palladium and tantalum surface. Tungsten metal does not diffuse or intake hydrogen, tantalum has some permeation of hydrogen, while palladium has higher permeation of hydrogen. Fast hydrogen atoms appear in a glow discharge cathode region because of acceleration of atomic and molecular ions and charge-exchange collisions or recombination on a cathode surface. The fast electronically excited hydrogen atoms manifest themselves in broadened wings of the spectral lines in a plasma emission.

4.1　Hydrogen Reflected Atoms

4.1.1　Tungsten and Tantalum Surfaces

Hα emission spectrum on tungsten and tantalum surface (within the plasma) is shown in Figure 4.1. Conditions include the floating potential and a target bias of -300 V. The potential held by an isolated substrate in the plasma is known as the 'floating potential', V_f, since the potential 'floats' to a value sufficient to maintain an equal flux of positive and negative species. This is compared with the target bias of -300 V. The upper two photos show the spectral profile for the tungsten and tantalum with floating potential and applied target bias. The bottom pictures are a zoom in of the profile. We could observe more from

molecular excitation and less Doppler broadening. This is observed in both conditions of the floating potential and with the applied target bias of -300 V.
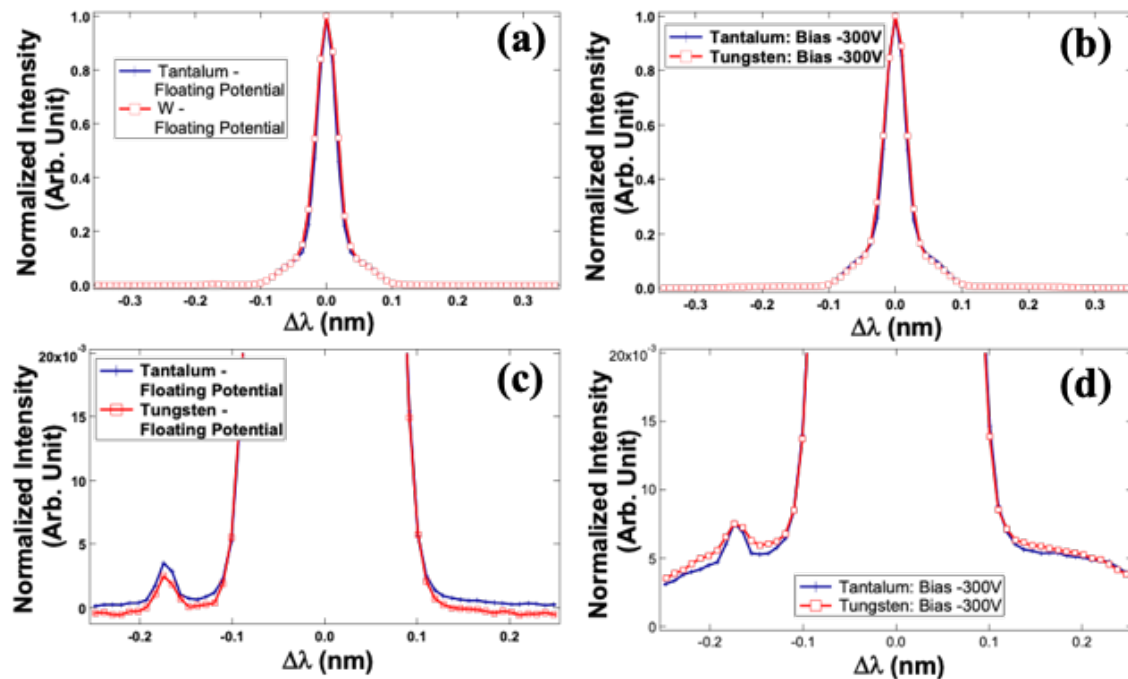
Figure 4.1–Hα *emission spectrum on tungsten and tantalum surface (within the plasma vicinity)*

In Figure 4.2 shows the Hα emission spectrum on tungsten and tantalum surface (peripheral region of the plasma) or outside vicinity of the plasma. Again, conditions include the floating potential and a target bias of -300 V. The upper two photos show the spectral profile for the tungsten and tantalum surface with floating potential and applied target bias while the bottom picture is a zoom-in of the profile. We could clearly see that the broadening of the spectral lines when a target bias is applied. The fast electronically excited hydrogen atoms manifest themselves in broadened wings of the spectral lines in a plasma emission. We used the wavelength shift formula, Eq. (3.1), to determine the regions where contributions from which ions are present. Thus, we have the following for hydrogen ions: H_3^+ range at $|\Delta\lambda| \leq 0.26$ nm , H_2^+ range at 0.26 nm $\leq |\Delta\lambda| \leq 0.37$ nm ,   and

H^+ range at $0.37 \text{ nm} \leq |\Delta\lambda| \leq 0.52 \text{ nm}$. Clearly, the results from the comparison between tungsten and tantalum show that obtaining the Doppler broadening at the peripheral region is achievable. Thus, the measurement method works by measuring the Doppler broadening at the outside vicinity of the plasma, perpendicular to the target.
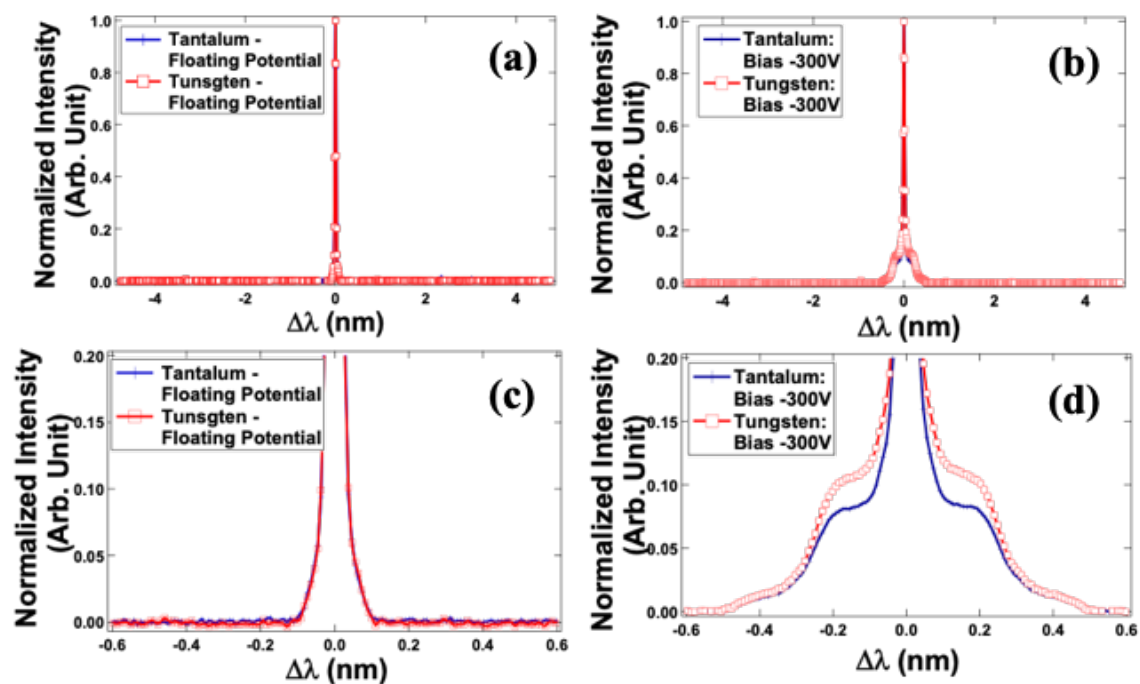
Figure 4.2–Hα *emission spectrum on tungsten and tantalum surface (outside the plasma vicinity)*

4.2   Modified Clamping Impact on Hydrogen Reflected Atoms

Now, currently a continuous water flow at the backside of the holder is usually maintained to avoid excessive heating of the target, but when the metal target bulks up from the backside cooling, heat accumulates more due to the plasma interaction (both from the plasma bombardment and removed cooling. For us to use higher bias voltages beyond -300 V, we designed and modified the clamp to ensure that all sides are attached to the backside

cooling. This difference is shown in Figure 4.3–Increasing target bias voltage impact on metal target. (a) -300 V and (b) -600 V as seen through a tube connected to an ICF 70 view port. We could see that by increasing the target bias voltage, the metal sheet bulks up thus less cooling is provided on the surface. This could greatly affect the resulting spectra for certain metals since higher temperature on the surface caused the metal to absorb more of the ions rather than reflect it.
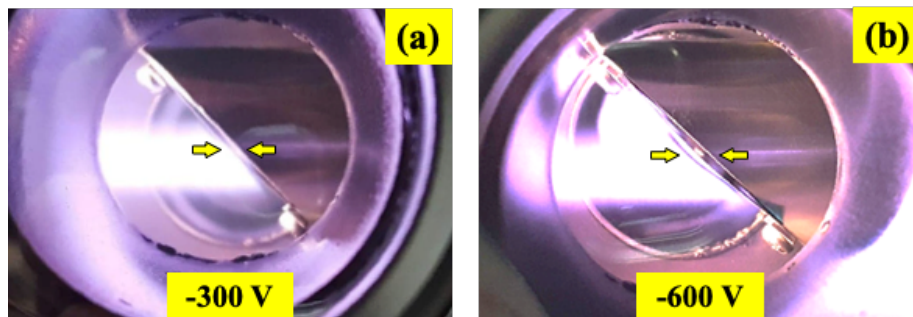
Figure 4.3–Increasing target bias voltage impact on metal target. (a) -300 V and (b) -600 V as seen through a tube connected to an ICF 70 view port

In Figure 4.4–Modification of clamp for metal targets. (a) Endpoint clamp, (b) Modified clamp, and (c) Modified clamp placed on target are shown. An endpoint fixture structure and a ring clamp structure were utilized to hold the metal sheet target in position of the water-cooled target holder in the original setup, Figure 4.4a. In the endpoint fixture structure or the endpoint clamp, small rectangular stainless-steel washers press the metal target to the water-cooled body by the screws. The second structure of modified clamp press the peripheral part of the metal target evenly with the ring fixture to realize a better heat transfer from the thin metal target to the surface of the water-cooled target holder, Fig. 4.4b. The effect on using those clamps on the Doppler-broadening of the hydrogen plasma on tungsten and palladium sheet metal targets are shown on the next slides.
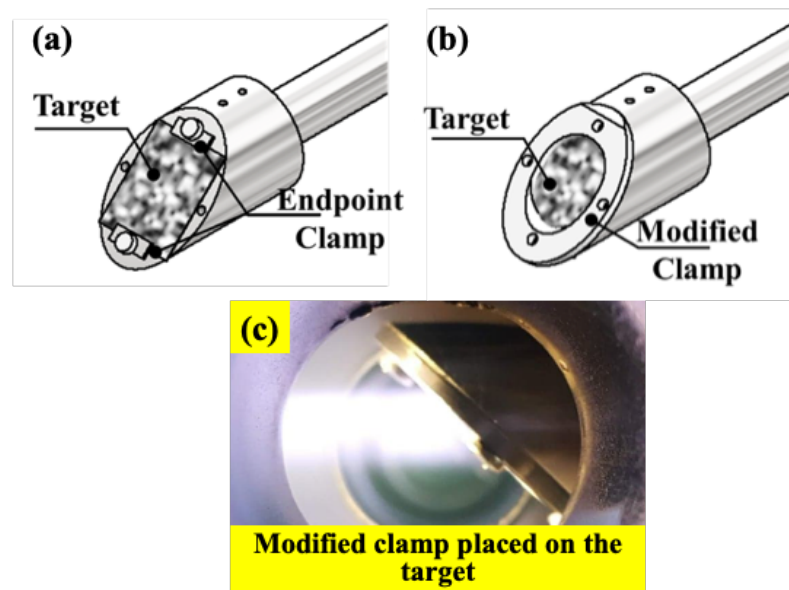
Figure 4.4–Modification of clamp for metal targets. (a) Endpoint clamp, (b) Modified

clamp, and (c) Modified clamp placed on target

4.2.1 Tungsten and Palladium Surfaces

The performance of the modified clamp is evaluated and compared when using palladium and tungsten as metal sheets. In Figure 4.5– Doppler broadening spectrum, in (a) linear and (b) semi-logarithmic scale, of the magnetized hydrogen plasma on palladium target under the endpoint clamp. The spectrum broadens with increasing negative bias voltages. Hydrogen reflection of tungsten and palladium have been compared between endpoint and modified clamp structures. The reflection characteristics were recognizable under a floating potential and increasing bias voltages with values of -100 V, -200 V, -300 V, -400 V, -500 V, and -600 V.

Fig. 4.5a shows the normalized intensity of the Balmer-α line spectrum emission of the peripheral region of the palladium target. Intensities are normalized at the central peak.

This illustrates an expansion of the Doppler-broadening due to the velocity distributions of hydrogen atoms excited by the collisions with H_2 molecules. Broadening of the spectral line is observed at increasing bias voltages. It also displays the blue and red wings of the Doppler shift in the negative and positive region of $\Delta\lambda$, respectively. As the target bias was raised to -600 V, the spectrum displays enlarged red and blue wings corresponding to the incident kinetic energies of hydrogen ions.

Comparing the -600 V and at the floating potential, -8.76 V, the former exhibits a wider line spectrum width than the latter. This indicates that the velocity distributions, from the dissociative excitation of H_2 molecules, is prominent at increasing negative bias voltages. Figure 4.5a also displays the blue and red wings of the Doppler shift in the negative and positive region of $\Delta\lambda$, respectively. Taking the spectra at -600 V, the blue and red wing under the endpoint clamp shows minimal difference. As the target bias was raised from -8.76 V floating potential up to -600 V, the spectrum displays enlarged red and blue wings corresponding to the incident kinetic energies of hydrogen ions. In addition, the ion species reflected are H^+, H_2^+, and H_3^+ can be observed (Figure 4.5a). However, to exhibit a clearer view of the reflected ions, a semi-logarithmic graph is displayed (Figure 4.5b). Ion species present in the plasma are H^+, H_2^+, and H_3^+ with the fraction composition changed due to particle recycling process at the target surface. The regions of the incident ions can be separated into three according to the general equation of wavelength shift, $\Delta\lambda$ in Eq. (3.1). For example, at -600 $V E_b$, only the hydrogen atoms produced by reflection of H^+ ions at the target forms the spectrum in the wavelength from 0.52 nm to 0.74 nm. The cut-off energies of atoms formed by the reflections of H_2^+ ions, and those of H_3^+ ions determine the wavelength range from 0.43 nm to 0.52 nm as the part constituted by reflections of H^+ and H_2^+ . The dissociative excitation of the background H_2 molecules produce light

emission forming the sharp central peak with $\Delta\lambda < 0.5$ nm.

Figure 4.5b shows the wavelength spectrum of light emissions from hydrogen atoms H^+, H_2^+, and H_3^+ reflections at Pd surface for the corresponding wavelength range. Intensities are normalized at the central peak. At the highest bias voltage of -600 V, the Doppler-broadening shoulder extended outward up to 0.7 nm, close to the value corresponding to 600 eV kinetic energy proton, due to excitation collisions with hydrogen molecules.
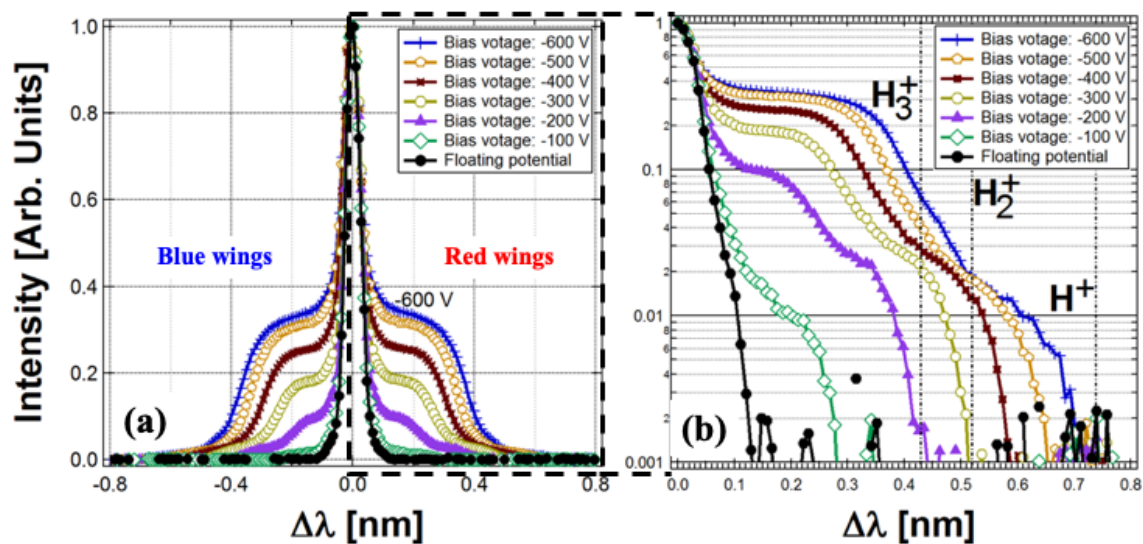
Figure 4.5– Doppler broadening spectrum, in (a) linear and (b) semi-logarithmic scale, of the magnetized hydrogen plasma on palladium target under the endpoint clamp. The spectrum broadens with increasing negative bias voltages.
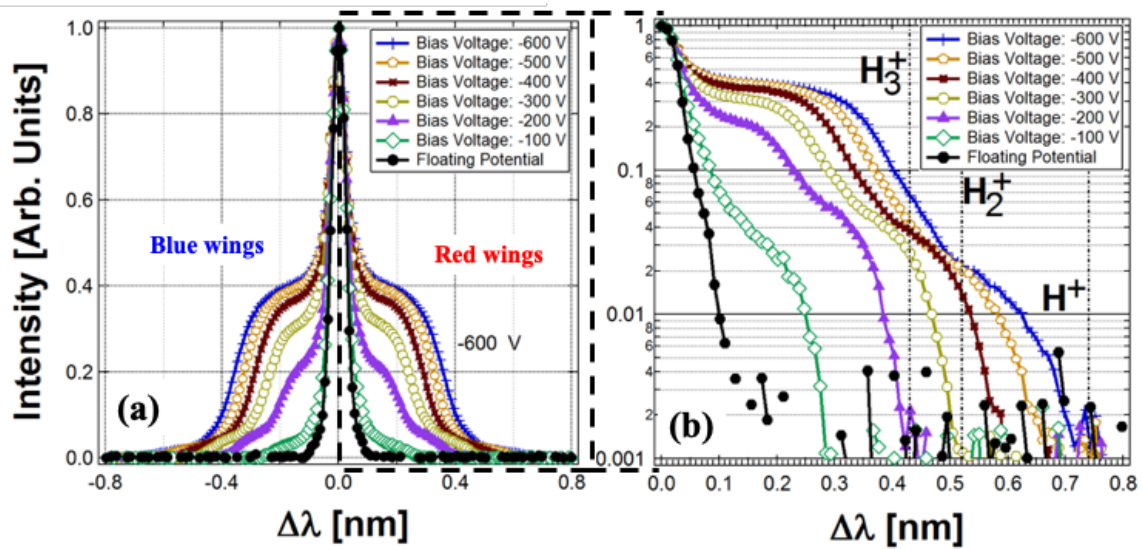
Figure 4.6– Doppler broadening spectrum, in (a) linear and (b) semi-logarithmic scale, of the magnetized hydrogen plasma on palladium target under the modified clamp. The spectrum broadens with increasing negative bias voltages.

Figures 4.6 a and b exhibits the palladium's hydrogen emission spectrum taken with the modified clamp at normalized intensity shown in linear and semi-logarithmic scale, respectively. From floating potential to -600 V bias voltage, a widening of spectrum is seen due to prominent presence of H_2 molecules dissociative excitation at increasing negative bias voltage (Figure 5a). The blue and red wing regions of the palladium target using the modified clamp demonstrates minute difference. The velocity distribution regions of H_3^+, H_2^+, and H^+ are seen in figure 5b. Similar cut-off energies at E_b = -600 V and expansion of the Doppler-broadening shoulder up to $\Delta\lambda = 0.7$ nm is present. Hydrogen ion reflection from tungsten and palladium metal sheets with both manifold clamps are seen in Figure 6a and b. Velocity distributions of the ion reflection is separated by bias voltages of E_b = -100 V and E_b = -600 V. From Eq. 1, at E_b = -100 V, the wavelength shift for H_3^+, H_2^+, and H^+ are $|\Delta\lambda| \leq 0.17$ nm, 0.17 nm $\leq |\Delta\lambda| \leq 0.21$ nm, and $|\Delta\lambda| \geq 0.30$ nm, respectively. On using

either the endpoint or modified clamp, there is no remarkable change on the velocity distributions H_2^+ and H^+ regions on tungsten surface. There is minimal change to no significant change in the H_3^+ region for E_b = -600 V and E_b = -100 V, respectively, on tungsten surface when using either of the two clamps.
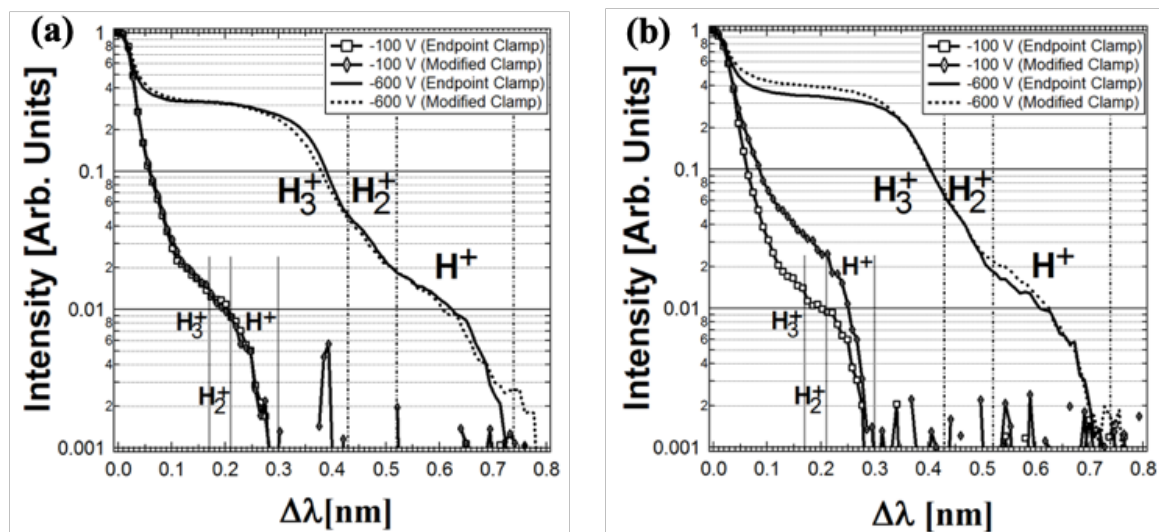
Figure 4.7– Doppler broadening spectra in both endpoint and modified clamp for (a) tungsten and (b) palladium. The spectral graph of -100 V and -600 V negative bias voltage are compared with each other using both clamps.

On the other hand, Figure 4.7 displays the comparison of the effect of both endpoint and modified clamps on the hydrogen reflection on the surface of the palladium metal sheet with bias voltages E_b = -100 V and E_b = -600 V. At E_b = -100 V, there is a prominent gap region wherein there is an observed lower emission spectrum on the endpoint clamp region relative to the modified clamp. Palladium with bias voltage E_b = -600 V also exhibited higher emission spectra, under the modified clamp, relative to the reflection distribution when endpoint clamp was used. Palladium show some enhanced signal on the H^+ and H_3^+

incident ion region when using a modified clamp. Modified clamp's impact on the emission spectra for palladium may indicate that the surface temperature on the metal sheets during bombardment also changed due to the full peripheral clamping of the second manifold. Placing a modified clamp, instead of an endpoint clamp, over the palladium metal created a direct contact with the surface backside cooling water. On the other hand, the endpoint clamp, where there is less cooling contact of the metal target, may create a mechanism where there are more adsorb molecules on the surface which may result to lesser hydrogen proton reflection. When using the infrared radiation thermometer, temperature was not completely detected for the modified clamp due to the 800 K detection limit for the infrared radiation thermometer.
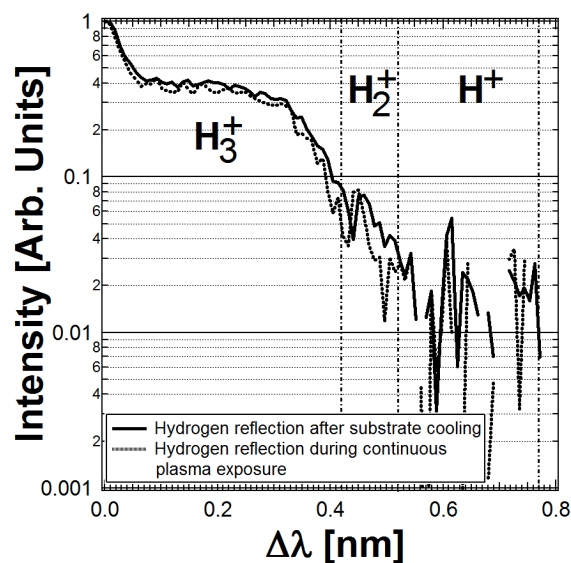
Figure 4.8– Hydrogen reflection on palladium after substrate cooling and exposure to continuous plasma under modified clamp.

The Figure 4.8 shows the hydrogen reflection on palladium metal sheet under modified clamp in certain cases wherein there is noticeable difference in hydrogen reflection for

diverse surface conditions. Conditions were compared from a spectrum captured during continuous plasma process and after substrate cooling effect were applied. After substrate water cooling, higher emission spectrum relative to the continuous plasma process is observed. There is a change in spectra with regards to relative temperature and condition of the metal surface target.

4.2.2 ACAT Simulation
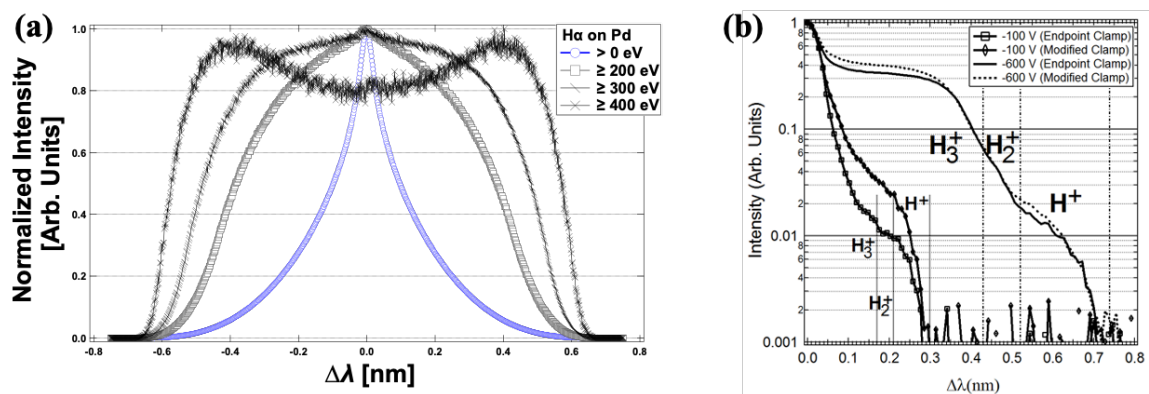
Figure 4.9– Reconstructed Hα Doppler broadening spectra on palladium surface
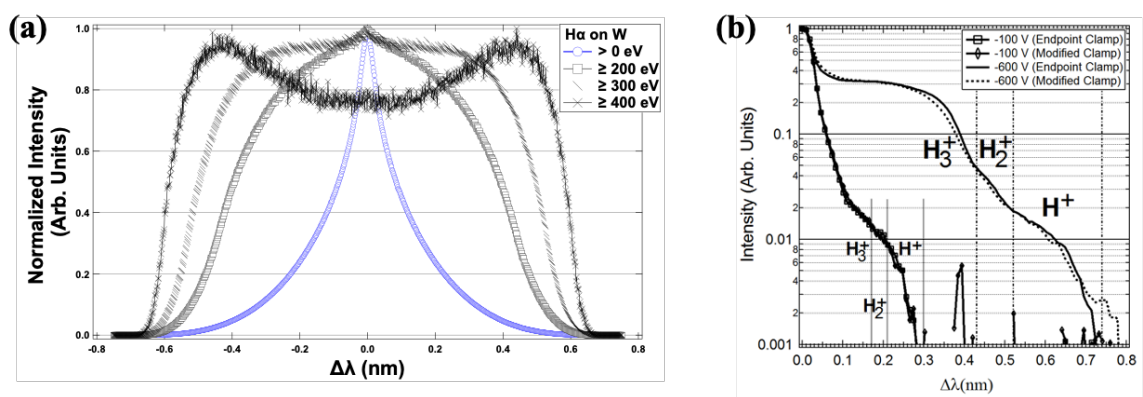
Figure 4.10– Reconstructed Hα Doppler broadening spectra on tungsten surface
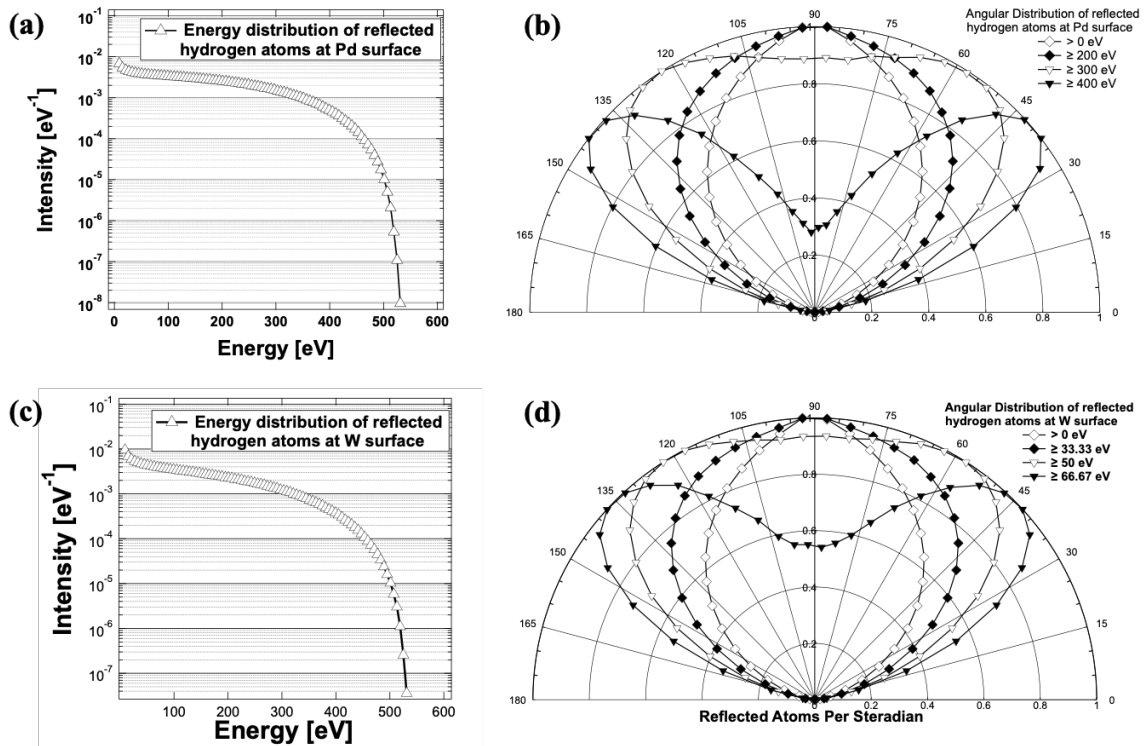
Figure 4.11– Reconstructed Hα Doppler broadening spectra on tungsten surface

4.3 Helium Reflected Atoms
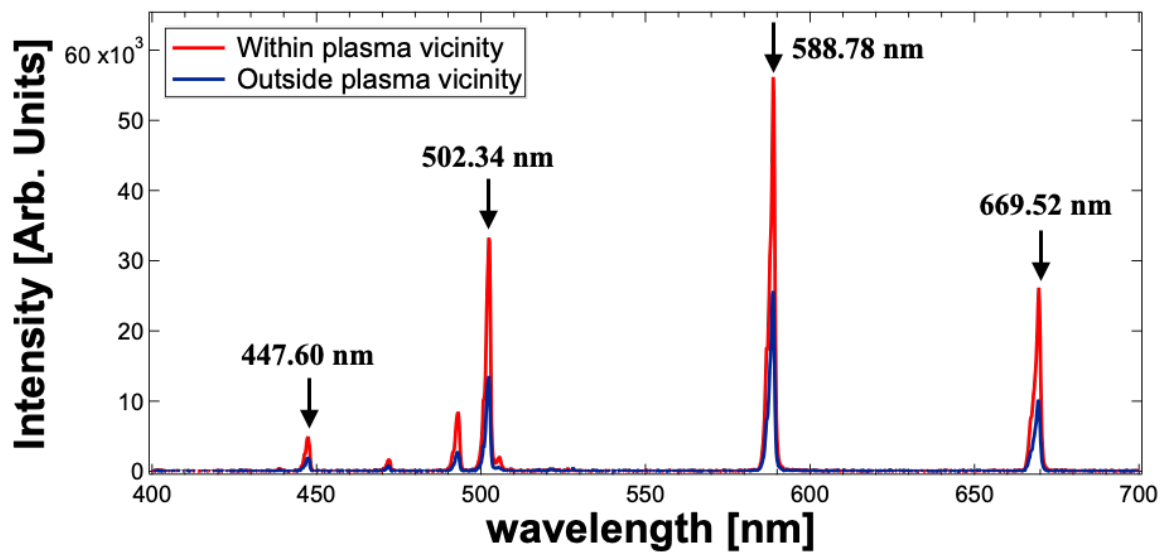
Figure 4.12– Helium spectra in the visible range

Objectives on the detection of the helium Doppler broadening on tungsten surface is to verify if the method of measuring the Doppler broadening perpendicular to the target is applicable to other gases (peripheral vicinity of the plasma) and here we will use helium gas on tungsten surface. We will also relate the results to the ACAT code.

Optical emission spectra of helium plasma on tungsten at different plasma vicinities is shown in Figure 4.12. Base from the energy level transition, we have here the wavelength number in the visible range within their transition levels shown in Table 4.1 – Helium wavelength table and those 2 wavelengths corresponds to the triplet transition while the other 2 for singlet condition.

Table 4.1 – Helium wavelength table

Wavelength	Transition
447.60 nm	$4^3D \rightarrow 2^3P$ (triplet)
472.03 nm	$4^3S \rightarrow 2^3P$ (triplet)
492.90 nm	$4^1D \rightarrow 2^1P$ (singlet)
502.34 nm	$3^1P \rightarrow 2^1S$ (singlet)
588.78 nm	$3^3D \rightarrow 2^3P$ (triplet)
669.52 nm	$3^1D \rightarrow 2^1P$ (singlet)

Base from the table, the wavelengths have transitions in the following manner: 447.2 nm ($4^3D \rightarrow 2^3P$), 501.6 nm ($3^1P \rightarrow 2^1S$), 587.6 nm ($3^3D \rightarrow 2^3P$), and 667.8 nm ($3^1D \rightarrow 2^1P$). Doppler broadening is mainly observed at the triplet state than on the singlet state. The wavelength shift (from Eq. 1), $\Delta\lambda$, at -600 V E_b, are 0.28 and 0.38, respectively for 587.6 nm and 667.8 nm as a sample. Two distinct broadening mechanisms are observed from the presence of two electrons that produces two metastable states in helium: singlet (2^3S) and triplet (2^1S) system. We want to know velocity distributions of reflected atoms from the surface of the metal targets of the Doppler broadening at these transitions.
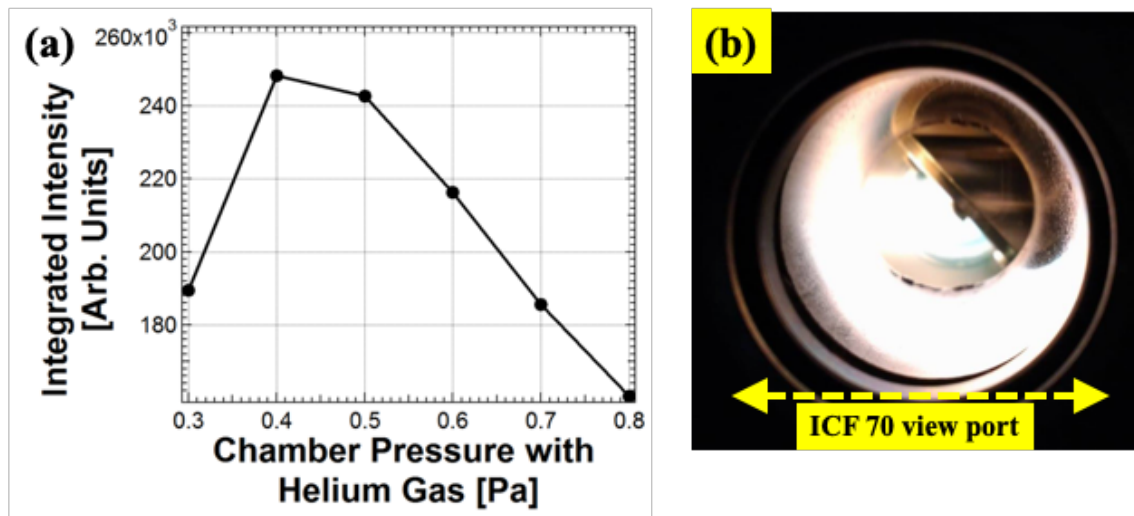
Figure 4.13– Helium plasma (a) integrated intensities at different pressure and (b) actual

ignition at 0.4 Pa chamber pressure (2 Pa helium pressure).

Before running the helium plasma, since helium has different characteristics with hydrogen, we cannot simply use the same pressure conditions from the previous setup. For this, we need to identify the pressure wherein we get the helium intensity the highest. To do this, we collected OES data, visible range, of helium plasma at different pressure ranges and compute for the integrated the intensities to obtain the optimum pressure value. The integrated intensities and actual helium plasma at the highest peak intensity is shown in Figure 4.13– Helium plasma (a) integrated intensities at different pressure and (b) actual ignition at 0.4 Pa chamber pressure (2 Pa helium pressure). Highest produced intensity is at 0.4 Pa chamber pressure or equivalent to 2 Pascal Helium pressure. We now see actual helium plasma with intense emission running at that pressure.

4.3.1 Doppler broadening of Helium Atoms Reflected on Tungsten Surface
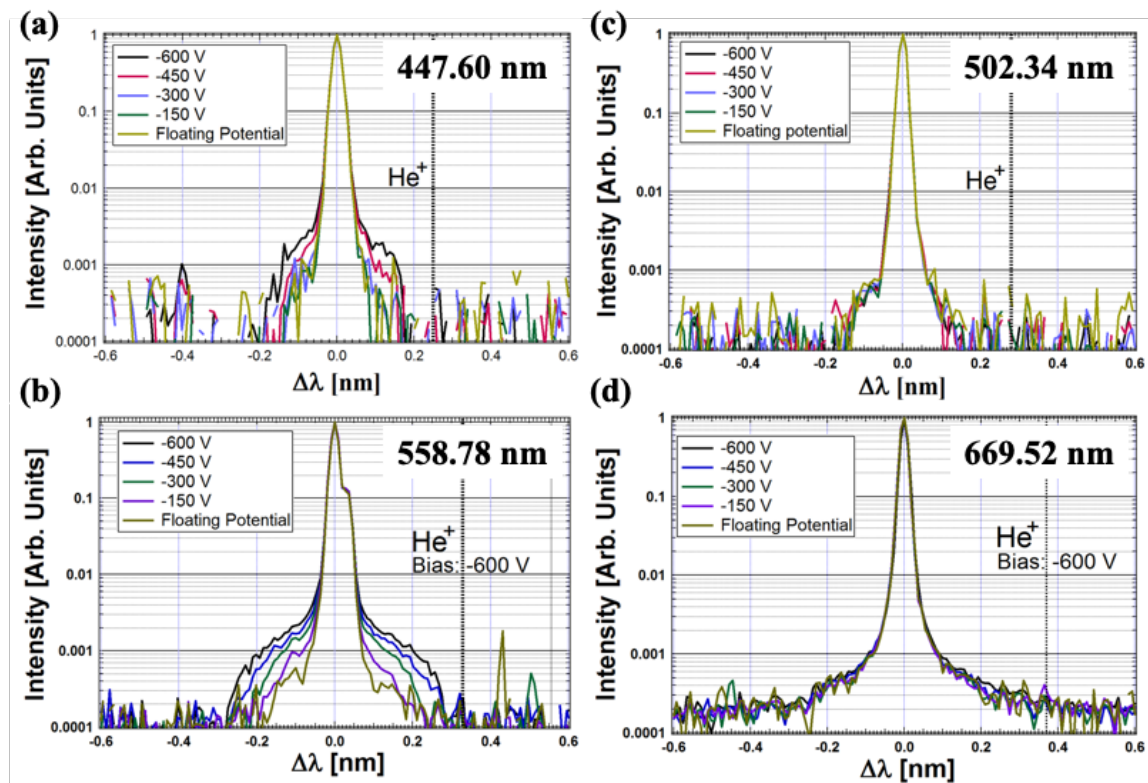
Figure 4.14– Doppler broadening spectra of helium plasma at different wavelengths. At triplet transition (a) 447.60 nm and (b) 558.78 nm while at singlet transition (c) 502.34 nm and (d) 669.52 nm)

Helium spectra of different wavelengths corresponding to triplet and singlet transitions are obtained and Doppler broadening is mainly observed at the triplet state than on the singlet state under a monochromator spectrometer. Expansion is directly proportional to the target potential. Increasing bias target also increases the expansion. For the singlet transitions, it seems that there is broadening, but not too prominent.

Possible model for helium plasma showing the difference in triplet and singlet state is shown in Figure 4.15– Possible Model for Helium Doppler Broadening. The second and more interaction with He* excited atoms produces the Doppler shift.
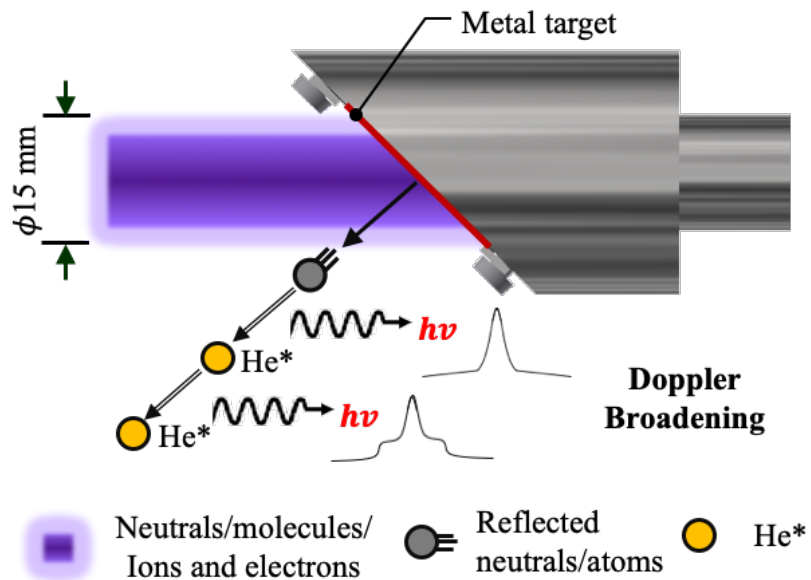
Figure 4.15– Possible Model for Helium Doppler Broadening

4.3.2 Surface Morphology of Helium Irradiated Tungsten Surface
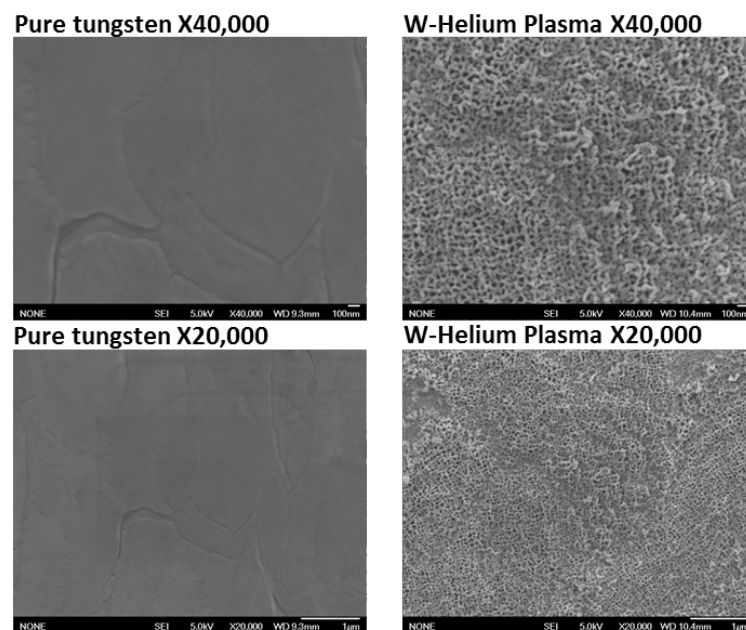
Figure 4.16– SEM of tungsten metal sheet exposed on helium plasma

Investigated SEM shows that an exposed tungsten surface on helium plasma is observed at 30 minutes exposure. The SEM image belows shows a target metal exposed at a discharge current of 1 A and have a target bias of 600 eV. There is presence of nanostructures after helium exposure. There is a possibility to pursue studies on the nanostructure formation on tungsten surface by helium plasma bombardment.

4.3.3 ACAT Simulation for Helium Plasma on Tungsten Surface
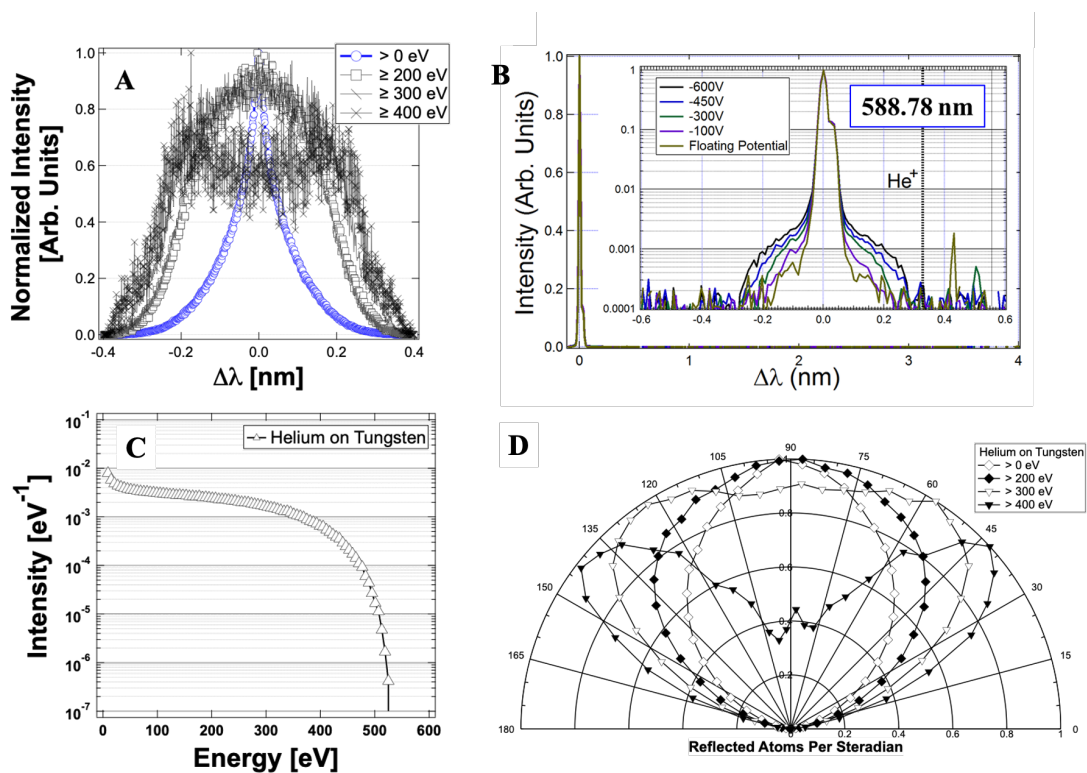
Figure 4.17– SEM of tungsten metal sheet exposed on helium plasma

Helium spectra of different wavelengths corresponding to triplet and singlet transitions are obtained and Doppler broadening is mainly observed at the triplet state than on the singlet state under a monochromator spectrometer. Expansion is directly

4.4   Summary

Observation of the Doppler mechanisms of hydrogen and helium plasma is observed. Plasma surface interaction is observed on surfaces like tantalum (Ta), palladium (Pd), and tungsten (W).

The measurement method of obtaining the Doppler mechanism is through the peripheral region perpendicular to the target is used and effective. Velocity distributions were computed for hydrogen [H_3^+, H_2^+, H^+] using the wavelength shift while experimental results are related to theoretical concepts using ACAT code.

Meanwhile, the surface temperature of the target mounted by the modified clamp cannot be evaluated as the temperature was below 800 K, which was the detection limit for the infrared radiation thermometer.

Interested in velocity distributions of reflected atoms from the surface of the metal targets of the Doppler broadening is using helium gas on tungsten. This verify that the method of measuring the Doppler broadening perpendicular to the target is applicable to other gases (peripheral vicinity of the plasma).

References

Doi, K., Yamaoka, H., Kenmotsu, T., & Wada, M. (2018). Spectroscopy Study of

    Hydrogen Atoms Reflected From Tungsten Surface in a Magnetized Plasma. *IEEE*

    Transactions on Plasma Science, 46(3), 482-488. doi:10.1109/tps.2018.2803753

Donets, E. D. (1998). Historical review of electron beam ion sources (invited). *Review of*

    Scientific Instruments, 69(2), 614-619. doi:10.1063/1.1148642

Tawara, H. (1964). Some Characteristics of a Duoplasmatron Ion Source. *Japanese*

    Journal of Applied Physics, 3(6), 342-346. doi:10.1143/jjap.3.342

Chapter 5 Spectroscopic Investigation of Molecular Species in Hydrogen Plasma

For molecular spectroscopic investigation, we want to verify if the gas heating is the cause for broadening of the central line. To do this, we determine hydrogen molecular temperature by investigating the rotational transition from the Fulcher-**α** region within the plasma vicinity. Since on the previous discussions, we know that the molecular excitations can be observed within the plasma volume.

Atomic and molecular processes in low pressure plasmas are examined in fusion edge plasmas. Both atoms and molecules can be excited through collisions in the plasma region. Molecule excitation is more complicated due to the additional quantum numbers, *v* and *j*, for both vibrational and rotational (rovibrational) quantum numbers, respectively. These values can identify rotational (T_{rot}) and vibrational (T_{vib}) temperatures to understand the underlying phenomena in the molecular and atomic excitations. Hydrogen forms a diatomic molecule in a room temperature laboratory condition and this paper limits the investigation to T_{rot}.

The temperature T_{rot} can be derived through examining and identifying the rovibronic emission lines from the hydrogen Fulcher-α bands (Shikima, 2007 and Fantz, 1998)In this paper, emission spectroscopy identifies the rovibronic lines of the hydrogen Fulcher-α $(d^3\Pi_u^- \rightarrow a^3\Sigma_g^+)$ Q -Branch at the near metal surfaces of palladium and tungsten targets immersed in hydrogen plasma.
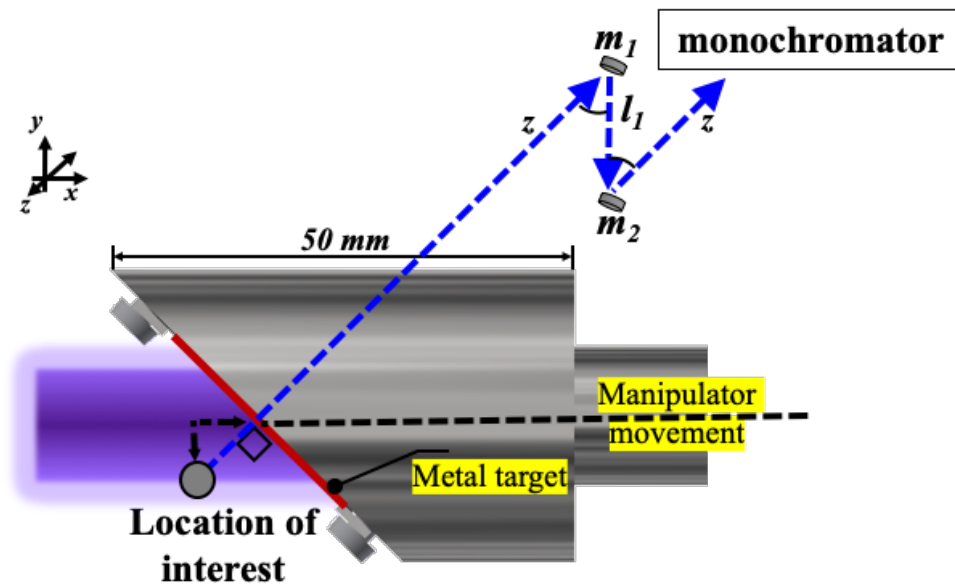
Figure 5.1– Schematic diagram of the location of interest (within the plasma vicinity) in the molecular spectroscopic investigation using hydrogen plasma.

In Figure 5.1 shows the location of interest ($x = 3$ mm). Schematic diagram of the location of interest in the spectroscopic investigation using hydrogen plasma. Metal targets, palladium and tungsten metal sheets (LxWxH: 25mmx25mmx0.1mm), were used. Optical guide mirrors were used to view the plasma from the spectrometer. Different negative bias voltages are applied at the substrate holder to investigate the spectral line emission with respect to bias changes. Bias voltages were valued at $E_b = -100$ V to -600 V.

Two spectroscopic devices have been utilized to observe the Balmer-γ, Balmer-β, Fulcher-α and Balmer-α lines of the hydrogen plasma on the metal surfaces. Optical emission spectra at the visible range of 400-800nm is used to detect the wider range of intensities of the hydrogen plasma. For finer structure conditions, a monochromator

spectrometer (spectral resolution: 0.23 Å) is used to examine the intensities and structure of the Q- branches in the Fulcher-a bands. The T_{rot} are then computed through the Boltzmann relation of the spectra measured.

5.1 Computation for the Rotational Transition

The intensities are related through Boltzmann approximation given by equation below (5.1),

$$I_{J'-J''} = g_{a,s} S_{J'J''} \lambda^{-4} \exp\left(\frac{-\mathrm{E}_{J'}}{k_B T_{rot}}\right) \tag{5.1}$$

Wherein $I_{J'-J''}$ is the intensity of the spectra with the J' as upper state and J'' as the lower state of the rovibronic line, which in this case is $J' = J''$ valued from 1 to 5. The constant $g_{a,s}$ equates to 1 or 3 for odd and even numbers, respectively, for the statistical weight of J' [3,4]. The Hönl-London factor is given by $S_{J'J''} = 0.5(2J + 1)$ while the wavelength is λ for a given intensity. $\mathrm{E}_{J'}$ is the energy of the upper state and can be expanded to $\left(\mathrm{B_e} - \alpha_\mathrm{e}(v' + 1/2)\right) * J'(2J' + 1)$ where $\mathrm{B_e}$ and α_e are rotational constants, v' is the upper state level $(v' = 0 - 4)$. The rotational transition is T_{rot} and k_B is the Boltzmann constant. Applying natural logarithm to the equation (5.1),

$$\ln\left(\frac{I_{J'-J''} g_{a,s}}{\lambda^{-4} S_{J'J''}}\right) = \frac{-\mathrm{E}_{J'}}{k_B T_{rot}} \tag{5.2}$$

5.2   Hydrogen Balmer Lines

In Figure 5.2, it shows the emission spectra of hydrogen plasma detected by a wide range visible spectrum device. Palladium has higher intensity relative to tungsten metal target. The Balmer-γ, Balmer-β, Fulcher-α and Balmer- α lines are observed though hydrogen plasma spectra on palladium is observed to have higher intensity at all regions. This could be attributed to the higher concentration of hydrogen in the vicinity of palladium.
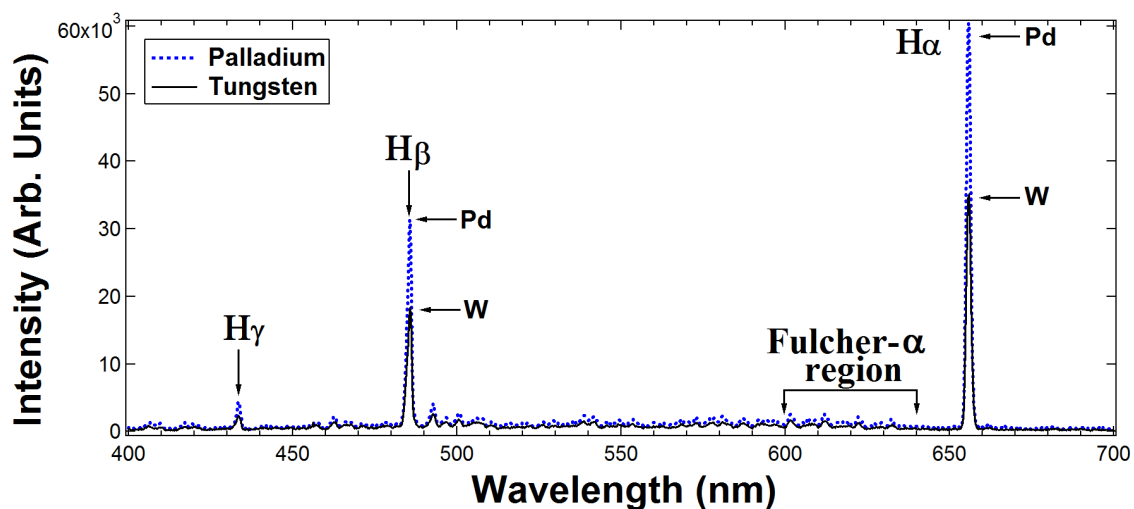
Figure 5.2– Optical emission spectra of hydrogen plasma on palladium and tungsten surfaces at −600 V bias voltage.

In addition, at increasing negative bias voltages, the Balmer region shows increase in intensity indicating higher plasma interaction within the region.

Figure 5.3 outlines the Balmer-γ, Balmer-β, and Balmer-α at increasing negative bias voltages. Although, at regions from $E_b = -200\,V$ to $-600\,V$, the intensity seems to have leveled and have only small increase. At each Balmer region, palladium has higher intensity than tungsten surface. This is also evident in the previous figure. Although palladium is known to absorb atomic hydrogen (H⁺) due to its material property, the molecule interaction may be different and could influence reactions within the plasma region.
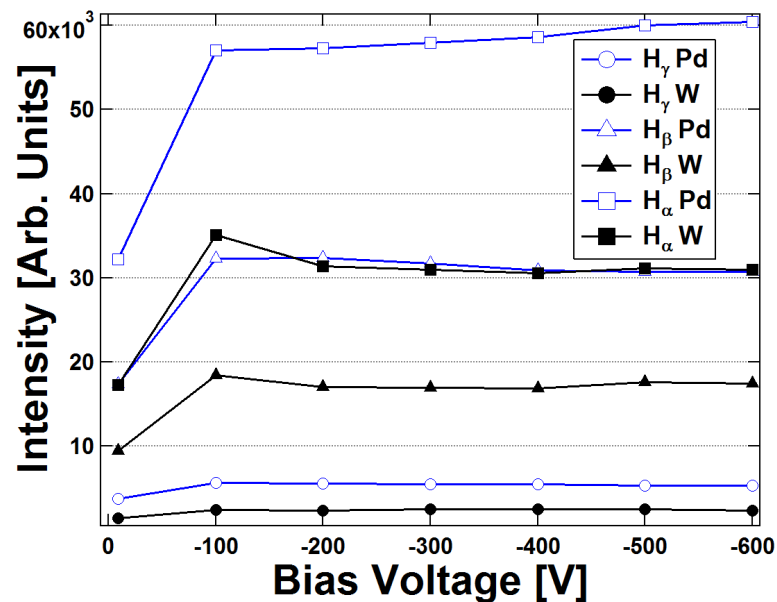
Figure 5.3– Balmer-γ, Balmer-β, and Balmer-α intensities of hydrogen plasma on metal targets.

Figs. 5.4 (a) and 5(b) show the Q branches between $v = v' = 0 - 6$ for palladium and tungsten, respectively. Regions between are also measured under wide range spectra. For Fig. 5(a), there is almost no distinction between the intensities at different bias voltages. For Fig. 5.4(b) intensity region, it shows decreasing intensity at increasing E_b, yet some

intensity lines are indistinguishable. Both figures show distinct peaks between $v = v' = 0 - 3$, although the robvibronic lines of each branch are impossible to tell apart.

Figure 5.4–Fulcher-α bands of the Q-branch line via optical emission spectroscopy of hydrogen plasma on (a) palladium and (b) tungsten surface.

The rovibronic lines can provide information on the rotational transitions and temperature of the interaction. On tungsten region, the Q-branches of (0-0)Q to (3-3)Q is clearly observed which pertains to the levels of $v = v' = 0 - 3$ for the rotational transition. In addition, the Fulcher-bands decreased in intensity as the bias voltage is increased to -600 V in this region (Fig. 5.4(b)). For Q-branches from (4-4)Q to (6-6)Q or $v = v' = 4 - 6$ depicted little change in intensity relative to the previous transitions on both figures (Figs. 5.4(a) and 5.4(b)).

To validate this, the Fulcher-α bands are further investigated at the wavelength region between 590-640 nm through the use a high-resolution spectrometer. This is shown in Figure 5.5– The measured intensities of the rovibronic lines (Q1-Q5) of the Q-branch of the hydrogen Fulcher-α diagonal band ($d^3\Pi_u^- \rightarrow a^3\Sigma_g^+$) of (a) $v = v'=0$ (b) $v = v'=1$

(c) $v = v' = 2$ and (d) $v = v' = 3$ on the near surface of tungsten metal sheet at floating potential and bias voltage *of* -600 V. Using a monochromator spectrometer, the fine structure of the branches from $v = v' = 0 - 3$, the rovibronic lines (Q1-Q5) of the Q-branch of the hydrogen Fulcher-α diagonal band $(d^3\Pi_u^- \rightarrow a^3\Sigma_g^+)$ identifies the (0-0)Q branch, $v = v' = 0$, 3(b) as (1-1)Q, $v = v' = 1$ (c) as (2-2)Q, $v = v' = 2$ and (d) as (3-3)Q, $v = v' = 3$ the rovibronic lines of the emission spectra for hydrogen plasma on palladium of the Fulcher-α band. was clearly observed as shown in Figure 5.5. The region showed increase in intensity at increasing negative bias voltages. Through the monochromator spectrometer, the rovibronic lines of the Fulcher bands were found more distinguished than using the wide range optical emission spectroscopy.

Eq. (5.2) is applied on Figs. 5.5(a) and (b) to compute for the rotational temperature derived from the Boltzmann condition. T_{rot} for $v' = 0$ values at $260 - 310$ K, $v' = 1$ values at $200 - 230$ K, $v' = 2$ values at $190 - 230$ K, and $v' = 3$ at $140 - 150$ K is derived from the rovibronic lines of hydrogen plasma on palladium. In addition, T_{rot} for $v' = 0$ values at $227 - 238$ K, $v' = 1$ values at $166 - 178$ K, $v' = 2$ values at $135 - 142$ K, and $v' = 3$ at $135 - 151$ K is derived from the rovibronic lines of hydrogen plasma on tungsten.
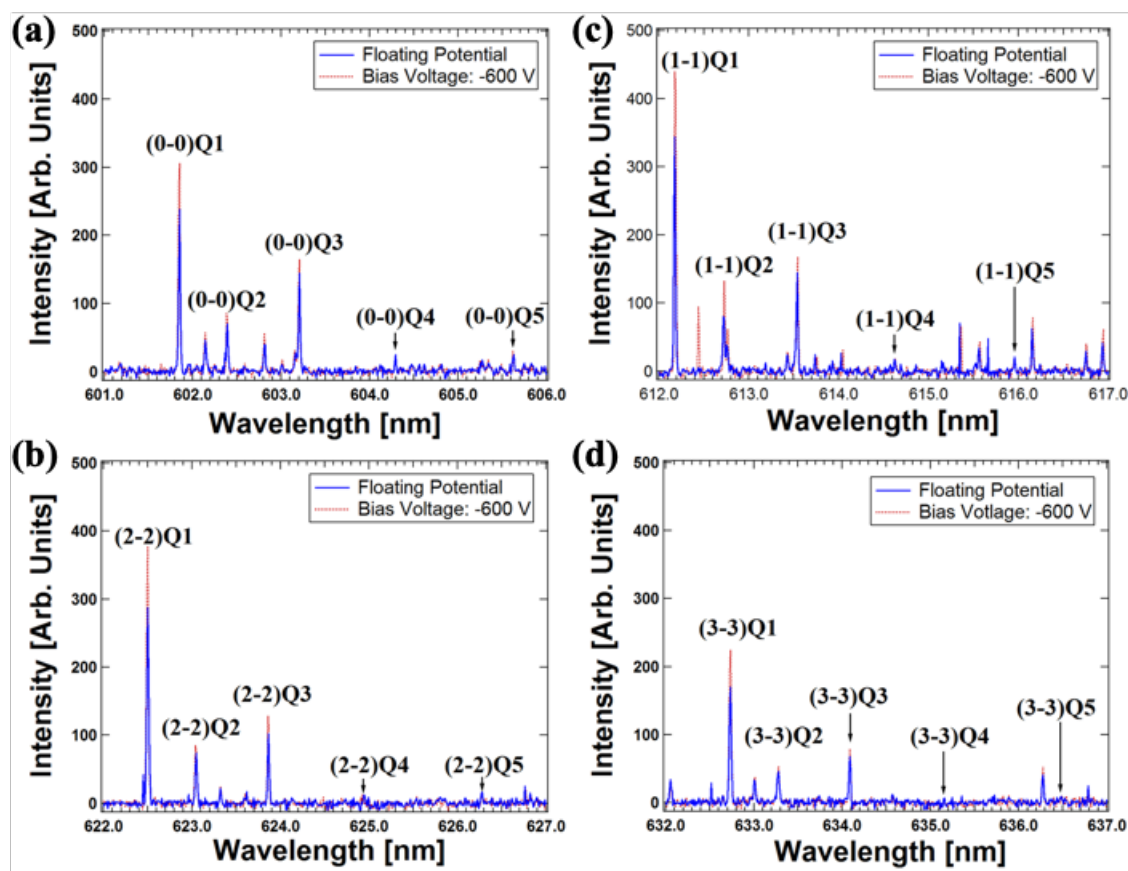
Figure 5.5– The measured intensities of the rovibronic lines (Q1-Q5) of the Q-branch of the hydrogen Fulcher-α diagonal band ($\mathrm{d}^3\Pi_\mathrm{u}^- \rightarrow \mathrm{a}^3\Sigma_\mathrm{g}^+$) of (a) $v = v' = 0$ (b) $v = v' = 1$ (c) $v = v' = 2$ and (d) $v = v' = 3$ on the near surface of tungsten metal sheet at floating potential and bias voltage of -600 V.

Overall, both sets of T_{rot} decreases as the rovibronic band level increases. Palladium, on all emission levels, have higher T_{rot} with respect to tungsten. Palladium seems to produce more excited molecules than tungsten during exposure to a hydrogen plasma.
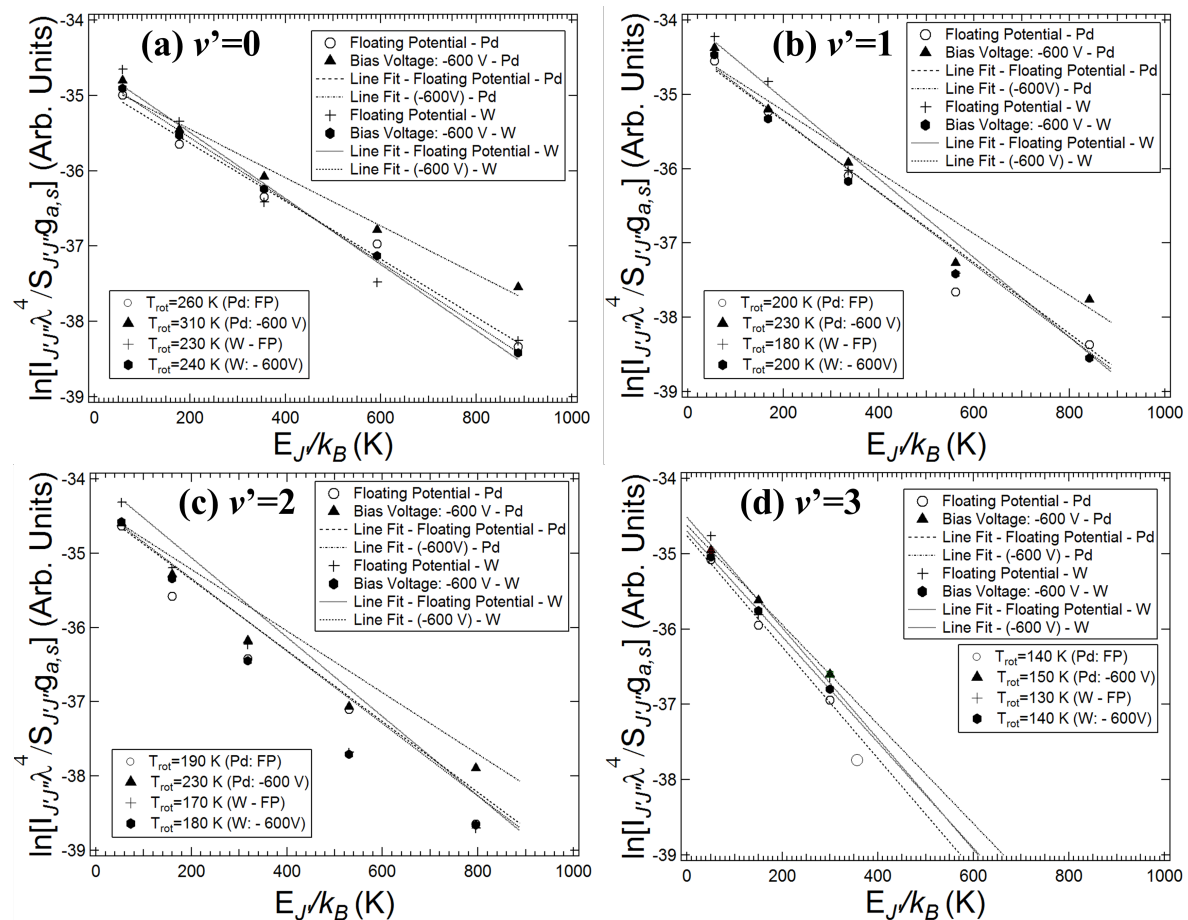
Figure 5.6– Computed T_{rot} from the rovibronic band lines $v = v' = 0 - 4$ of the hydrogen plasma on metal targets, palladium and tungsten.

5.3 Corrected formula for rotational transition

The corrected formula for Eq. (5.2) is given by Eq. (5.3)

$$I_{J'-J''} = g_{a,s} S_{J'J''} \lambda^{-4} exp \left(\frac{-hcE_{J'}}{k_B T_{rot}} \right) \qquad (5.3)$$

The corrected formula for Eq. (5.1) if given by Eq. (5.4)

$$\ln\left(\frac{I_{J'-J''}\lambda^4}{g_{a,s}S_{J'J''}}\right) = \frac{-hcE_{J'}}{k_B T_{rot}} \tag{5.4}$$

Recomputed T_{rot} from the rovibronic band lines $v = v' = 0$ of the hydrogen plasma on metal targets, palladium and tungsten is given by Figure 5.7– (Corrected) Fulcher-α bands of the Q-branch line via optical emission spectroscopy of hydrogen plasma on (a) palladium and (b) tungsten surface. The changes where the abscissa is different. Since there was a conversion factor for the wavelength and the computed slope relation for trot was different. Hence, we can now see here a much higher rotational temperature. Yet. This is not too high to indicate that the gas heating effect is the source for the broadening of the central line at lower energies.

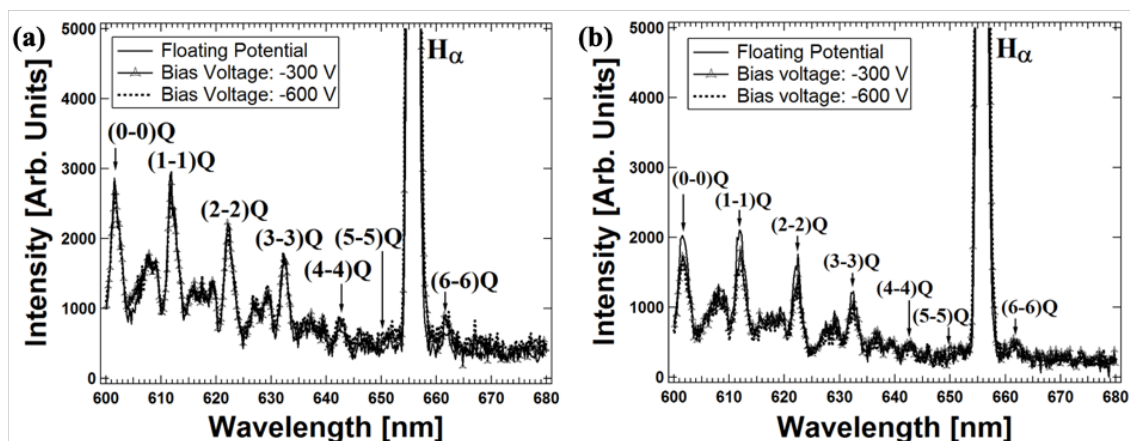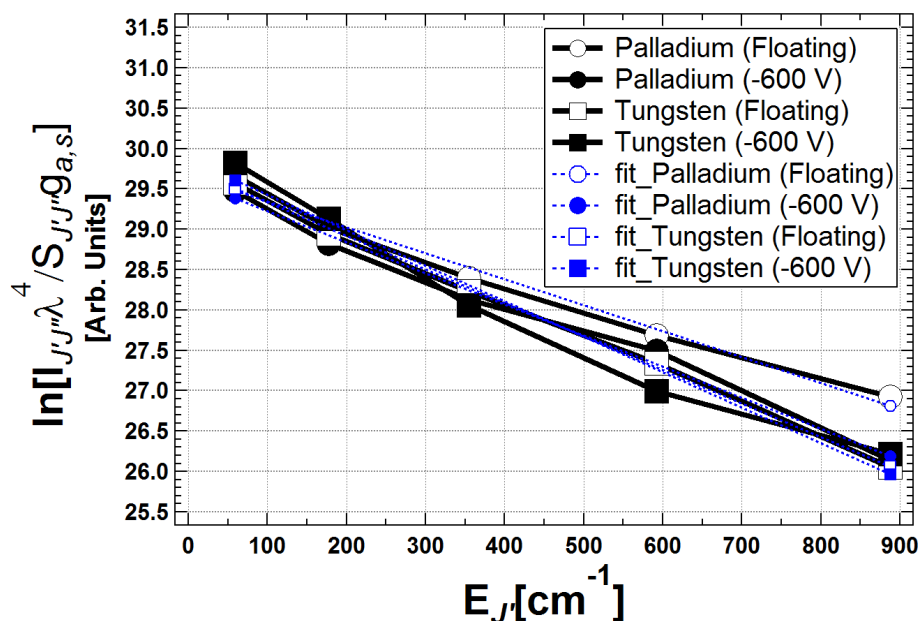Figure 5.7– (Corrected) Fulcher-α bands of the Q-branch line via optical emission spectroscopy of hydrogen plasma on (a) palladium and (b) tungsten surface.

Table 5.1 – Table of corrected rotational temperature

Condition	Slope	T_{rot}
Tungsten (Floating)	.0044	308.96 K
Tungsten (-600 V)	.0042	323.67 K
Palladium (Floating)	.0038	357.74 K
Palladium (-600 V)	.0032	424.82 K

5.4 Summary

We were able to determine the molecular species by obtaining the Fulcher-α band of the emission spectra of hydrogen plasma. Investigation using a monochromator spectrometer (spectral resolution of 23 pm), is preferred to be used. The computed the rotational temperature, T_{rot}, and resulted to around 300 K~420 K at level $v' = 0$. Values are not that high for the Gas heating effect to be cause of the observed line spectrum broadening and other underlying mechanism can be the source.

The observed spectrum showed a substantial broadening that could not be explained by the particle reflection at the target; the spectrum showed broadening at the skirt part even at low (less than 150 eV) hydrogen ion bombardment energy. The large plasma radius and the exposed target area may cause the velocity and the angular distributions of both incident and reflected hydrogen particle to vary and thus can enlarge the broadening of the Hα line spectrum. To investigate the cause of the broadening at lower energy for tungsten, the thick plasma needed to be narrowed down. Thicker beam produced from the previous plasma cathode can hit at any place. Ions and neutrals are running an oblique angle which may be reflected to the broadening of the central wavelength. Meanwhile, A smaller diameter plasma is preferred because the line of sight

for the spectroscopic measurement should be set as close to the particle emission point as possible

A duoplasmatron source can produce intense plasma that can pass through an aperture less than 0.13 mm diameter. This small size plasma ball can produce both ions and electrons depending upon the extraction voltage. It was then discussed that to do this, we have to modify the current ion source from a DC plasma cathode setup to a duoplasmatron ion source configuration.

References

Jr., D. C., Barreta, L. G., Rocha, C. J., Santos, A. M., & Bertran, C. A. (2008). Determination of liquefied petroleum flame temperatures using emission spectroscopy. *Journal of the Brazilian Chemical Society, 19*(7), 1326-1335. doi:10.1590/s0103-50532008000700015

Fantz, U., & Heger, B. (1998). Spectroscopic diagnostics of the vibrational population in the ground state of and molecules. *Plasma Physics and Controlled Fusion, 40*(12), 2023-2032. doi:10.1088/0741-3335/40/12/003

Herzberg, G. (1989). *Molecular spectra and molecular structure: Spectra of diatomic molecules*. Florida: Krieger Pub.

Honda, Y., Álvaro-González, A., Nezu, A., & Akatsuka, H. (2017). Spectroscopic Examination of Fulcher-α Band of Microwave Discharge H 2 -D 2 and H 2 -He Plasmas. *Energy Procedia, 131*, 312-318. doi:10.1016/j.egypro.2017.09.456

Iza, F., & Hopwood, J. (2004). Rotational, Vibrational, and Excitation Temperatures of a Microwave-Frequency Microplasma. *IEEE Transactions on Plasma Science, 32*(2), 498-504. doi:10.1109/tps.2004.826145

58

Kado, S., Yamasaki, D., Iida, Y., & Xiao, B. (2004). Anomaly in the P- and R-Branches in the Spectra of Hydrogen Fulcher Band Emission. *Journal of Plasma and Fusion Research, 80*(9), 783-792. doi:10.1585/jspf.80.783

Majstorović, G. L., Šišović, N. M., & Konjević, N. (2007). Rotational and vibrational temperatures of molecular hydrogen in a hollow cathode glow discharge. *Plasma Sources Science and Technology, 16*(4), 750-756. doi:10.1088/0963-0252/16/4/009

Shikama, T., Kado, S., Kuwahara, Y., Kurihara, K., Scotti, F., & Tanaka, S. (2007). Fulcher-α Band Spectra in Mixed Hydrogen Isotope Plasmas. *Plasma and Fusion Research, 2*. doi:10.1585/pfr.2.s1045

Chapter 6   Duoplasmatron Ion Source

Fundamental processes in plasma material interactions are often investigated using a linear device with an electron emission cathode for quasi-steady-state operations (Donnets, 1998 and Fantz, 1998). A device using high-temperature tungsten cathode is used to understand the Hα line spectrum profiles. These profiles are base from the particle reflection coming from hydrogen plasma reflected on metal surfaces. (Donnets, 1998). The line of sight for the measurement was set outside of the plasma to reduce noise due to photon emissions from the plasma. The measured spectra showed clear broadening corresponding to the velocity distributions of reflected particles when their incident energies were higher than 200 eV. To measure the broadening below 200 eV, a duoplasmatron ion source was assembled to realize a thinner plasma.

6.1   Duoplasmatron Ion Source

6.1.1 System Concept

Several types of ion sources have been explored, developed, and engineered throughout the years to investigate different atomic and molecular ion reaction/interaction on different a variety of surfaces (Donets, 1998 and Tawara, 1964). A duoplasmatron ion source is developed with the addition of a hollow cathode for higher extraction efficiency. A high-resolution spectrometer is used to obtain the particle emission from the tungsten metal target surface. The hydrogen ions reflected on the tungsten surface is investigated and discussed. In, Figure 6.1, the typical design for the duoplasmatron ion source is shown

as initial blueprint for the design (Mason, 2016). Typical inlet is shown for the gas source which reacts to the DC powered tungsten cathode. This in turn creates a plasma which then extracted through the intermediate electrode. Plasma thickness is reduced depending on the hole diameter.
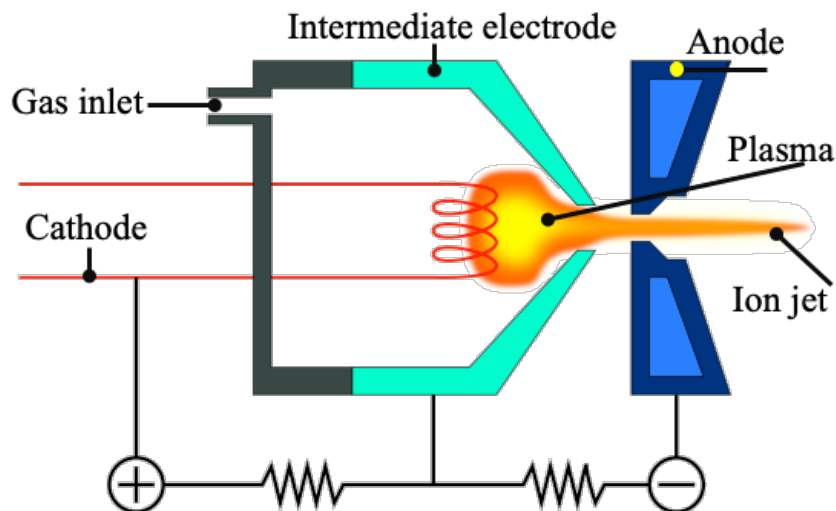
Figure 6.1– Typical design of duoplasmatron ion source

6.1.2 Initial Designs

A duoplamatron ion source was developed to replace a standard high temperature cathode source from the previous setup assembled by Doi (2018). This modification produces positive ions that bombards the tungsten (0.1mmx24mmx25mm) metal sheet. Hydrogen gas (0.8–1.0 HPa) are ionized by the electrons produced from the tungsten (Φ.40x155 mm) filament's thermionic emission. The plasma then passed through the intermediate electrode, made of iron, that was added in front of the cone-shaped conduit, Figure 6.2. The neodymium ring magnet (N40, Φ40xΦ30xΦ10mm), with an average magnetic residual flux density of 12.75 KGs, surrounds the intermediate electrode to further

enhance the plasma excitation. An Fe-anode is isolated from the electrode and is used used to extract ions through positive bias voltage application. A hollow cathode is positioned few millimeters away from the anode. This constricts and focuses the plasma column at the center.

Now we replaced the ion source head only. The duoplasmatron ion source should function as both positive extraction and plasma cathode than extract electrons. The ion source device is being modified to introduce positive ions to probe the surface under plasma irradiation.
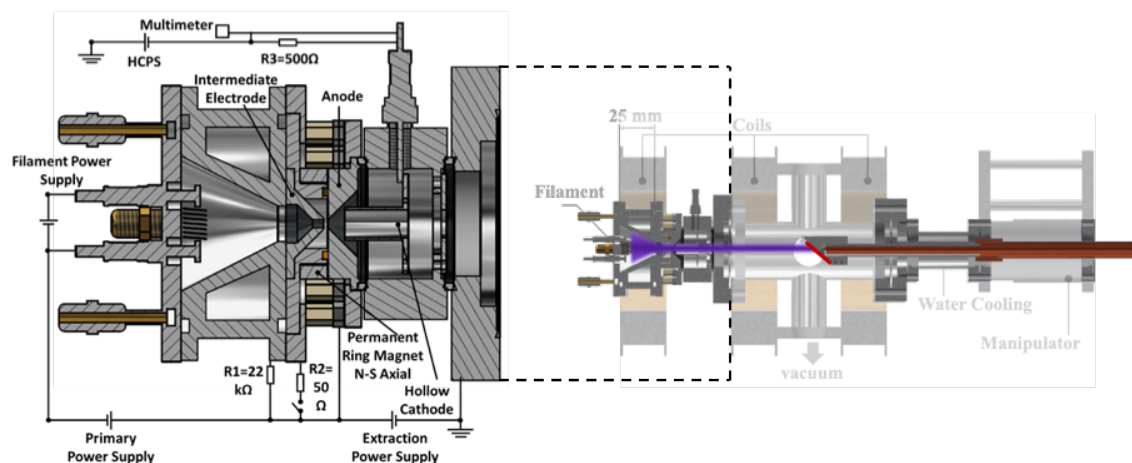
Figure 6.2– Duoplasmatron ion source initial design

Duoplasmatron ion source will provide a flux of ions to the surface of the target metal. As the ions travel through the plasma volume, the space-charge blow-up of the ion beam is mitigated to make transport in the energy range from 100 eV to 1 kV possible. Both reflection component, as well as sputtering atoms, will be measured with the high-resolution spectrometer. However, we were not able to utilize this setup and decided to move forward with a different design.

6.1.3 Duoplasmatron Ion Source as a Plasma Cathode Device

A duoplasmatron ion source was developed to replace a standard high-temperature filament driven plasma cathode source from the previous setup, Figure 3.3–DC plasma cathode device cross section. Figure 6.3 shows the experimental arrangement with the duoplasmatron plasma source that looks nearly identical to the original setup used for plasma bombardment onto a fuzzy tungsten surface (Doi, 2018). This is because the main part of the plasma source for both setups is covered by the first electromagnet. In fact, even though the structure of the current duoplasmatron is more complicated than the previous plasma cathode, the length was much shorter; the length of the duoplasmatron plasma cathode from the filament to the extraction electrode is 86 mm while that of the previous plasma cathode from the filament to the flange of the downstream chamber is 144 mm.

Two more electromagnetic coils produce a linear magnetic field to guide the ionizing electrons wherein the three electromagnetic coils to provide a linear magnetic field. There is a port for vacuum pumping. An ICF 70 viewing port is placed for spectroscopic and luminosity intensity measurements while the manipulator for target holder is used to adjust the target distance from the center chamber. A target electrical bias connection which ranges up to -600 V is used. An in and out water-cooling ports for backside cooling of the target is provided.
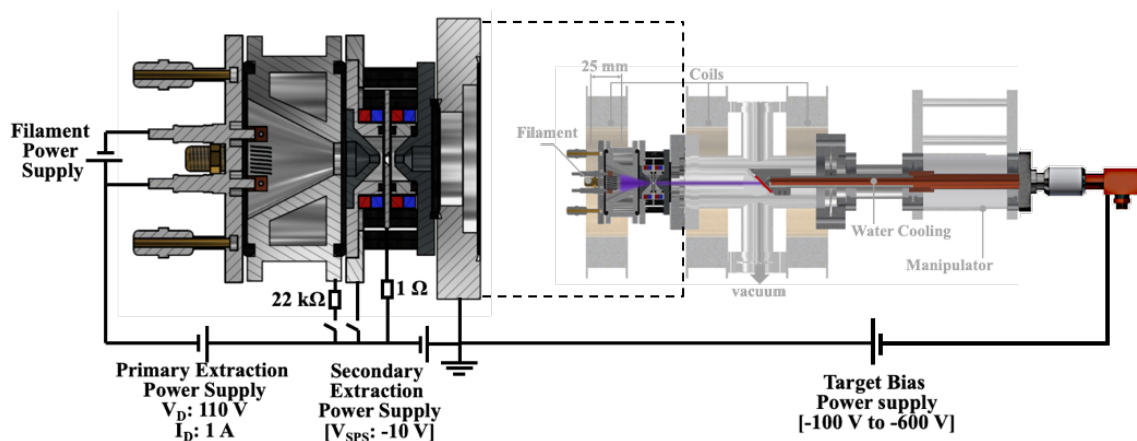
Figure 6.3– Duoplasmatron ion source (electrical schematic diagram for plasma cathode)

Figure 6.4 shows the structure of the duoplasmatron plasma source. The operation of the source is illustrated using the alphabet A through F indicated. The horizontal and vertical orientation of the device is labeled as the *x*-axis and *y*-axis, respectively. **1** The filament power supply (FPS) for primary electron emission. **2** Primary discharge power supply (PPS) for primary discharge current production. **3** Secondary power supply (SPS) for secondary extraction. **4** Target bias power supply (TBPS). **5** primary switches. **6** Secondary switch. A pair of current feed-through sustains a 0.40 mm diameters tungsten filament, **A**, for thermionic emission of ionizing electrons. Tungsten filament (a 7-turn coil with a 6 mm diameter of 0.4 mm diameter 155 mm length tungsten filament). The discharge is initiated between the filament and the conical water-cooled stainless-steel (SUS304) electrode, **B**. The ignition anode is a cone-shaped conduit with dimensions of ϕ 83 mm X ϕ 13 mm X 33 mm. Once the discharge is initiated, the plasma electrons penetrated a region formed by a mild steel made intermediate electrode, **C**. The intermediate electrode is made of iron and has the volume of conical shape with the dimensions of ϕ 6 mm X ϕ 3mm X 10.5 mm. The electrical register connected to the cone shaped conduit biases the conduit

at a floating potential drawing little discharge current from the primary discharge power supply (PPS). Thus, the conical electrode ignites the plasma, but the main part of the discharge current runs between the tungsten filament and the intermediate electrode. The current from the tungsten filament cathode passes through a 3 mm diameter hole opened at the center of the intermediate electrode and touches down the anode plate, **D**, as the switch connecting the intermediate electrode to the anode is opened.
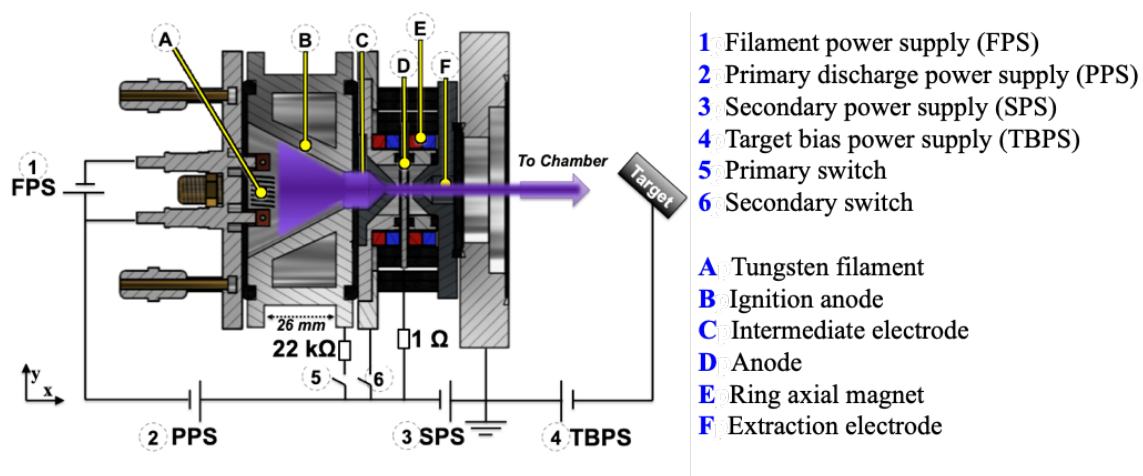
Figure 6.4– Duoplasmatron ion source design

The anode is an SUS304 circular plate with a 2 mm diameter tapered aperture. **E** Ring axial magnet (North-South *x*-axis orientation, $\phi 40$ mm X $\phi 30$ mm X 10 mm). A pair of Nd-Fe ring magnets creates an intense magnetic field (estimated to be more than 4.5 kG [6]) in the region between the intermediate electrode and extraction electrode, **F**, to compress magnetically the plasma reaching the anode. This process completes the formation of a duoplasmatron plasma, and the dense plasma is ready to be extracted from the mild steel made extraction electrode with the inner volume $\phi 6$ mm X $\phi 3$ mm X 6.5 mm facing the anode. The PPS delivers a discharge current, I_{D1}, of typically 1 A and discharge

voltage, V_{D1}, of 110 V in a usual operation. Filament power is maintained at 184-186 W to sustain the discharge current of 1 A.

Both electrons and positive ions can be accelerated from the plasma source by simply switching the polarity of the secondary discharge power supply, SPS. The spacing between the plasma source anode and the extraction electrode is 1 mm while the diameter of the extraction hole is 3 mm. The 2 mm thickness extraction electrode is tapered by a 45-degree angle at the side facing the extraction electrode. This part of the anode works as the expansion cup to control the local plasma density low enough to extract charged particles (van Steenbergen, 1965). A strong inhomogeneity in the axial magnetic field intensity is created in the extraction region, because the extractor is made of magnetic material (mild steel). A double layer is known to be produced in this magnetic field configuration (Plamondon, 1988) and the plasma self-bias effect was often observed depending upon the polarity of the secondary discharge power supply; the plasma source acquires the potential as the power supply is protected against the reverse electrical current flow.

The extracted charged particle beam forms a plasma in the downstream area where a magnetic field is induced by electromagnets. A stable plasma is produced as electrons are extracted from the plasma source with input coil current, I_{coil}, from 7.5-15 A corresponding to the magnetic field intensity from 140 to 280 G. The plasma guided by the magnetic field extends up to the target normally located at 12 cm downstream of the extraction electrode, which is referred to as the standard position. The surface of the target can be adjusted by linear motion feedthrough along the direction of the magnetic field, while the target surface is observed from the tangential direction perpendicular to the field through two viewing

ports with the center axis aligned to the surface center of the target located at the standard position.

The previous figure shows the electrical wiring connection is shown when electrons are extracted from the duoplasmatron source. The SPS extracts electrons from the plasma cathode forming a sharp downstream plasma. A sheet metal target is attached to a water-cooled target support to be irradiated the surface by the plasma from the direction 45-degrees to the surface normal. The target can be electrically biased with respect to the plasma using a Target Bias Power Supply (TBPS).
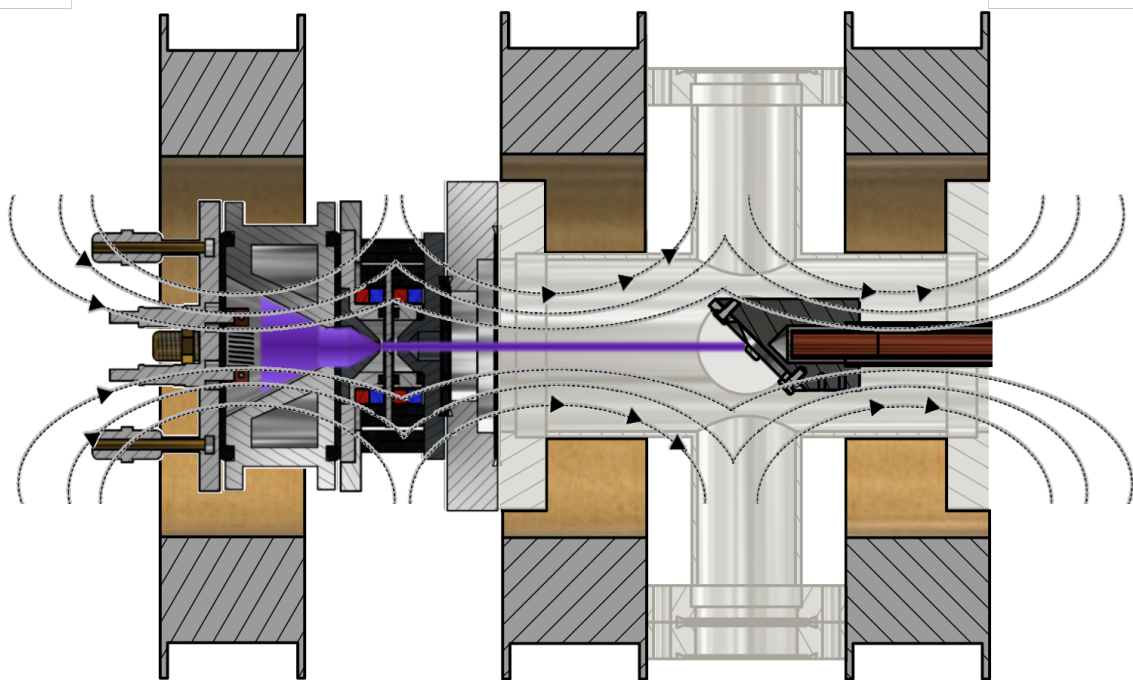
Figure 6.5– Duoplasmatron used as a plasma cathode with an applied external magnetic field

Duoplasmatron used as a plasma cathode with an applied external magnetic field. Figure 6.5– Duoplasmatron used as a plasma cathode with an applied external magnetic

field is shown. Aside from the two permanent magnets we have inside the source, we can still use the external electromagnetic coils to compress the ion beam more. The variation of increasing electromagnetic coil and its impact on the ion beam will be shown in the succeeding chapters.

6.2 Duoplasmatron Ion Source Discharge Characteristics

6.2.1 Duoplasmatron Ion Source as a Plasma Cathode

The operation of the duoplasmatron as an ion source will be discussed later. The operation of the source as the plasma cathode is explained how to obtain the set original goal: production of sharp plasma. Once the duoplasmatron discharge is established after opening the secondary switch, 6 in Figure 6.4, the hydrogen pressure was adjusted from 0.17 to 0.6 Pa to see the effect for the dependence of the primary discharge current upon the filament current.

The result in Figure 6.6 shows the same primary discharge current was obtained gradually up to 0.17 Pa hydrogen pressure for the same filament heating power, while more filament heating power was necessary for operation at higher pressure. As a substantial increase in heating power was required for operation with hydrogen pressure higher than 0.2 Pa, the pressure was kept at this value to examine the performance of the cathode. As we apply the secondary discharge voltage, V_{SPS} between the duoplasmatron anode and the extraction electrode, electrons are extracted to form an ionizing electron beam toward the downstream of the extractor.
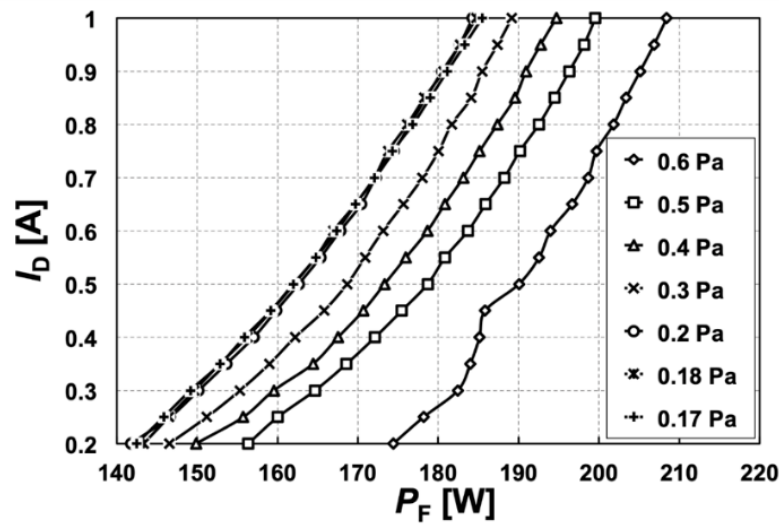
Figure 6.6– Discharge Current (A) vs Filament power (W) for varying chamber pressure (hydrogen). [I_{D1}: 1 A, V_{D1}: 110 V, I_{coil}: 0 A, V_{SPS}: 0 V].

The current flowing the secondary discharge power supply, I_{D2}, was almost equal to the discharge current, I_{D1}, driving the duoplasmatron discharge. In Figure 6.7, the discharge current ratios, I_{D2}/I_{D1}, and the floating potentials of the tungsten target are plotted as functions of V_{SPS} for two values of discharge current: $I_{D1} = 0.5$ A and $I_{D1} = 1.0$ A. As shown in the figure, the same magnitude of electrical current flows the secondary discharge power supply, even with no bias current. The ratio almost equates to 1 even for increasing V_{SPS}.

The magnetic field intensity that guides I_{D1} through the anode to make it as I_{D2} is far much greater than the linear magnetic field induced by electromagnets. Figure 6.7 data shown was taken without inducing current to the electromagnets, but the identical characteristics were measured when the current was applied to the electromagnets. The produced plasma downstream of the duoplasmatron anode is biased negatively using a

secondary power supply (V_{SPS}) to transfer the electron to the chamber. The positive terminal of the V_{SPS} is grounded to the chamber. The current ratio I_{D2}/I_{D1} was measured to be slightly smaller than one when the primary discharge current was kept at 0.5 A, while it tended to be slightly larger than one at higher V_{SPS} with $I_{D1} = 1.0$ A. The accuracy in the measurement for taking data of Figure 6.7 was one percent. The reason for the observed data scattering is attributable to the change in discharge condition when the V_{SPS} is varied.

The floating potential of the tungsten target became more negative with the increasing V_{SPS} and larger I_{D1}. Based upon the data of hydrogen ionization cross-section [9], the secondary discharge potential was set at 70 V in the following experiment to make the electron impact energy above the maximum for the cross-section to ionize hydrogen.
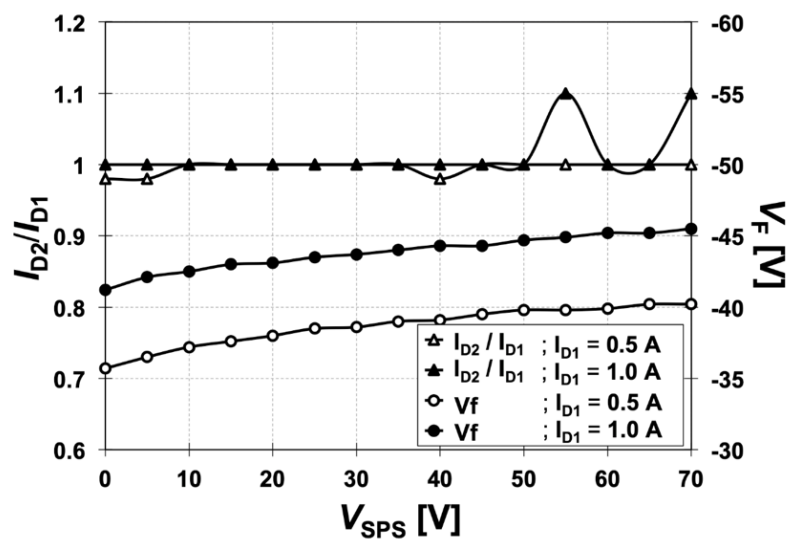
Figure 6.7– Discharge characteristics of duoplasmatron plasma cathode source I_{D2}/I_{D1} vs V_{SPS} and V_F (secondary axis) vs V_{SPS} [I_{D1}: 1 A, V_{D1}: 110 V, I_{coil}: 0 A, V_{SPS}: 0-70 V negative bias].

6.2.2 Duoplasmatron Ion Source as a Positive Extraction

Once the SPS electrically reconnected, with positive bias input voltage and negative bias grounded to the chamber, to extract positive ions was connected, there appeared an 80 V self-bias potential between the extractor and the duoplasmatron anode as shown in Figure 6.8– Duoplasmatron as a positive extraction source for increasing target bias. By applying an extraction potential, the extraction current immediately saturated at 70 mA above 400 V for 0.5 A discharge current. Further increase in extraction voltage resulted in a breakdown at the extractor (only 1 mm gap between the anode and the extractor) and the operation above 400 V was unstable.

However, because of the observed characteristics of positive voltage self-bias, positive ions are expected to pass through the plasma expansion area downstream of the anode. They produced a dilute plasma downstream, and the tungsten target showed a negative floating potential indicating the ion beam reaching the target was smaller than the thermal electron current from the ion beam produced plasma. Part of the reason for the inefficient positive ion transport down to the target is the large beam divergence of this type of ion source for the operation with a low extraction potential (Kuzumi, 2020). The extraction geometry must be modified if the present source will serve as a positive ion source.
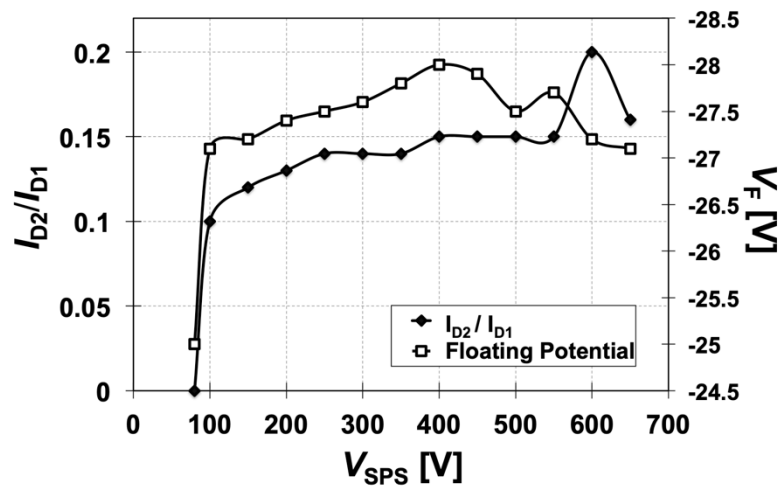
Figure 6.8– Duoplasmatron as a positive extraction source for increasing target bias

6.3   Luminosity Profile Intensity

6.3.1   Concept Technique

The tungsten target was withdrawn out of the region observable through the viewing port. All pictures were taken in a batch process to make sure that all analyzed locations are the same. The image data are converted to 8-bit grayscale and pixel data were integrated to construct a luminous intensity distribution along the y-axis perpendicular to the magnetic field line of force. The diameter of the plasma glow column was more than 1 cm in the previous experimental system with the tungsten filament excited plasma cathode depending on magnetic field compression. Note that Figure 6.9 is tilted by 90-degree to quantify the

luminous intensity distribution for the measurement of the radius of the ionizing electron flowing channel.
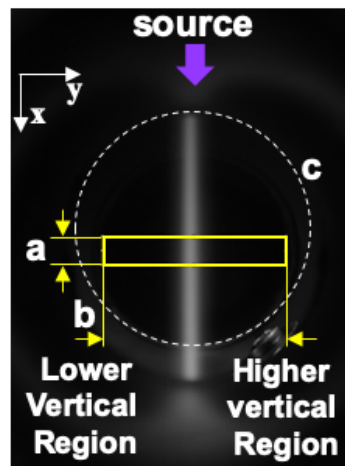
Figure 6.9– Duoplasmatron as a positive extraction source for increasing target bias

As indicated in the figure, a luminous intensity distribution is obtained by averaging the signal along the width indicated by the label 'a' extending in x, or the horizontal direction. The label 'b' is assigned to show the direction toward the bottom, where the surface of the tungsten target is located away from the center of the viewing port. The vertical y coordinate has the origin at the plasma center and is more negative toward the label 'b'. The circle 'c' is drawn as a reference of the 34 mm diameter opening on the stainless-steel chamber welded to the tube to hold the ICF-70 size viewing port flange.

6.3.2 Luminosity Profile Intensity Results
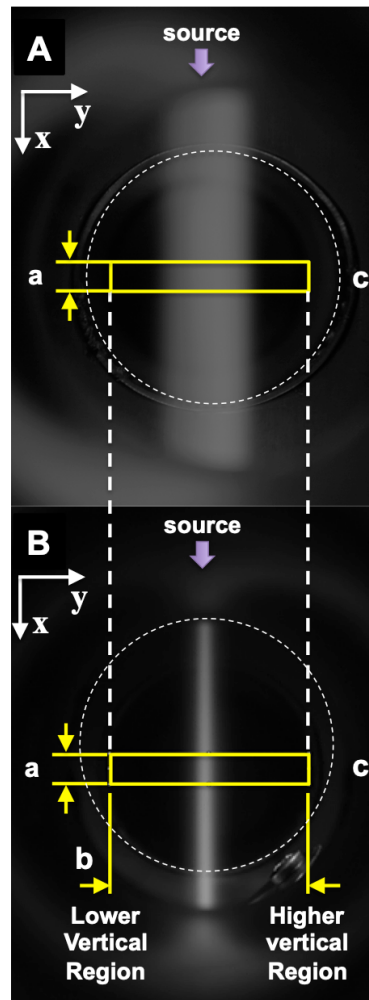
Figure 6.10– Plasma glow for the **A**: previous plasma cathode and **B**: Duoplasmatron plasma cathode [I_{D1}: 1 A, V_{D1}: 110 V, I_{coil}: 15 A, V_{SPS}: -10 V, and no target bias]. The plasma flow is from the arrow indicated (*x*-axis). **a**: Region for averaging of the plasma drift direction with grayscale unit scale. **b:** Lower region indicates the lower *y*-axis of the plasma region **c:** Reference of the 34 mm diameter (actual measurement) circle opened on the inner wall of chamber connected to a stainless-steel tube holding the ICF-70 viewing port at the other end.

The luminous intensity distributions in the *y*-direction are plotted for different values of coil current to produce linear magnetic field keeping I_{D1} at 1.0 A. Voltage for SPS is -10 V. No distinct change in intensities for SPS input until -70 V. Hydrogen pressure is still sustained at 0.2 Pa. The magnetic field intensity, *B*, at the center of the tungsten target surface can be expressed by $B = 18.7 \text{ X } I_{coil}$ with I_{coil} being the current supplied to the electromagnets.

Figure 6.11– Luminosity profile at varied secondary discharge voltages at increasing electromagnetic coil current. **A** 0-7.5 A electromagnet current input and. **B** 10-15 A electromagnet current input. [I_{D1}: 1 A, V_{D1}: 110 V, and V_{SPS}: -10 V].

Figure 6.11shows that the system can guide the plasma down to the target position with only less than a 2.5 mm displacement even without inducing the current to the electromagnets. This is because the pair of toroidal magnets forming the duoplasmatron magnetic field generates a straight magnetic field along the axis. The misalignment of the duoplasmatron field axis with respect to the linear magnetic field axis is estimated to be less than 1.4-degree.

As the electromagnetic coil current is increased, the profile starts to focus even with 2.5 A. A clear sharpening of the profile is observed starting at 10 A current to the electromagnets as indicated in Figure 6.11B. The maximum luminous intensity was observed at 7.5 A electromagnetic coil current. The reason for observing the maximum intensity at a reduced magnetic field intensity is unclear at this moment. A strong gradient of axial magnetic field intensity also exists at the region downstream of the extraction electrode like in the gap between the plasma source anode and the extractor. The formed double layer can enhance the local plasma loss at a higher field intensity, but this assumption should be tested by investigating the local plasma inside the constricted region. Increase in secondary extraction voltages did not affect the luminous intensity profile; the peak intensities and the width of the profiles were similar. Above more than 10 A coil current, a sharp plasma-glow column of less than 2.5-3.0 mm radius was realized.
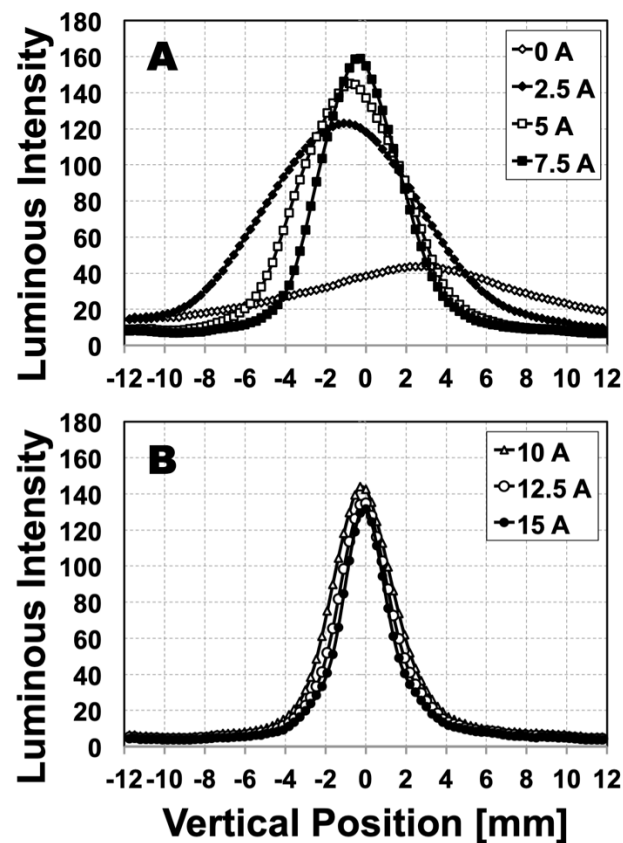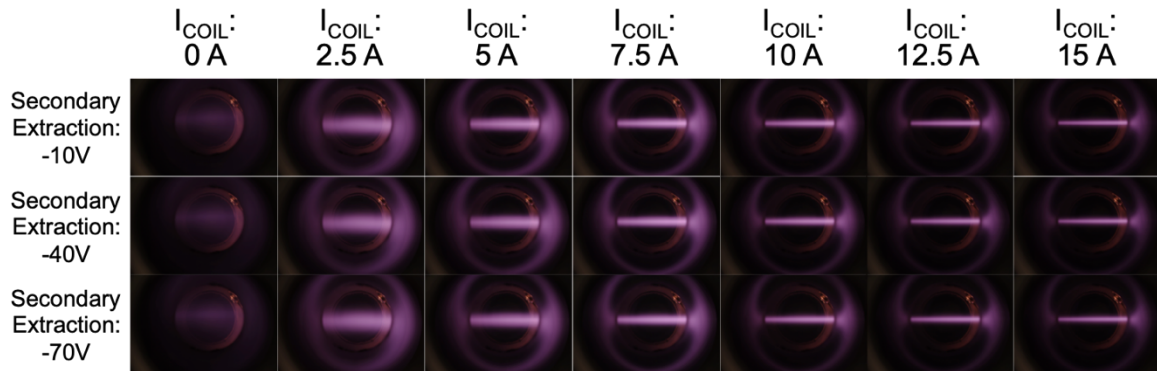
Figure 6.12– Luminosity profile at varied secondary discharge voltages and increasing

electromagnetic coil current.

From Figure 6.11, checking the other luminosity profiles at increasing secondary voltages, we have Figure 6.12. Visually checking at increasing secondary voltages, almost no significant difference between the intensity of the beams. Figure 6.13 shows the luminosity profiles. It shows the profile intensities of each secondary extraction voltage from -10 V to -70 V. shows almost no significant difference.
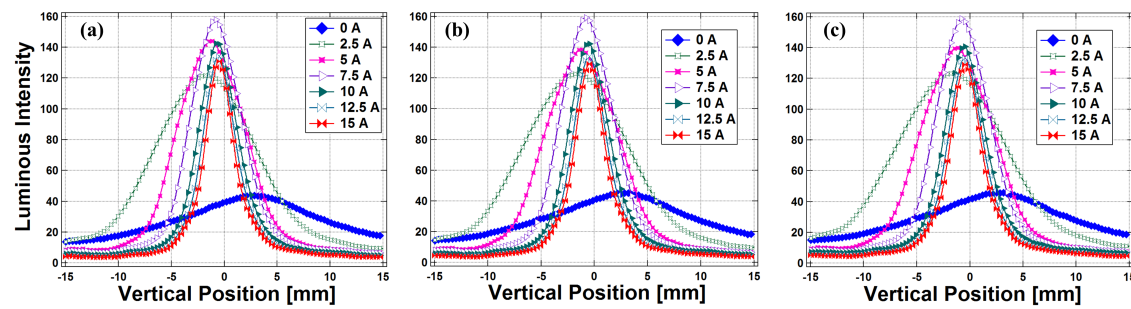
Figure 6.13– Varying Coil Current and Extraction Voltage Luminosity Profile

Applying different target bias voltages with secondary voltage of -10V, we have Figure 6.14. Its equivalent profile intensity is in Figure 6.15. It shows that at 15 A coil current at -600 V, almost the plasma is too thin. Also, noticing between 5 A and 10 A coil

current, the plasma is observed to be slightly terminated starting at -300 V and -400 V (yellow arrow). When -600 V is applied, visually, plasma termination is much observed (orange arrows).
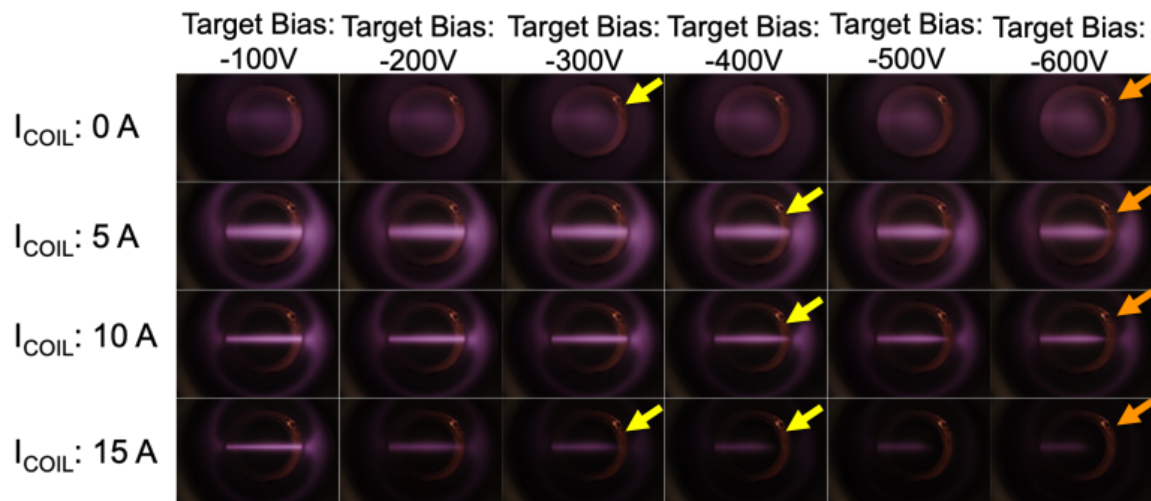
Figure 6.14– Luminosity profile at varied electromagnetic coil current and target bias voltage [I_{D1}: 1 A, V_{D1}: 110 V, I_{COIL}: 0-15 A and V_{SPS}: -10-70 V].

At 15 A coil current shows decreased in the intensity profiles. A strong gradient of axial magnetic field intensity also exists at the region downstream. We can clearly observe the start of the plasma termination at the regions (pointed by yellow arrows) to the orange ones. This plasma termination will be discussed in the next chapters.
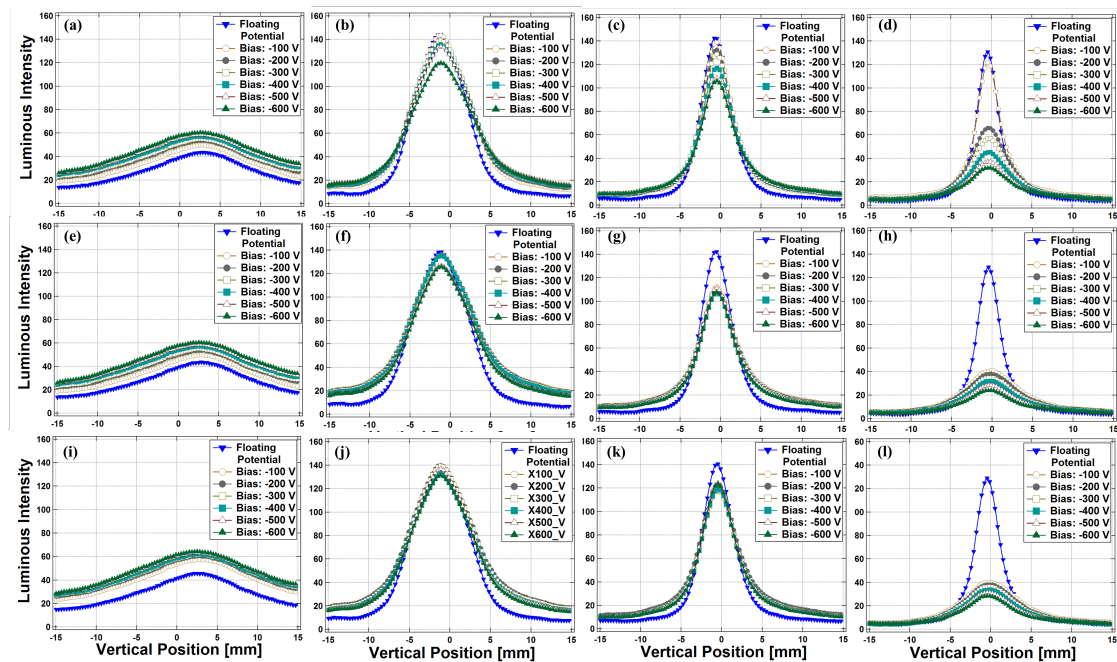
Figure 6.15– Varying Target Bias and Varying Coil Current Luminosity Profile

To further see the plasma termination through the luminosity profile intensities, Figure 6.16 shows the luminous profile intensities of the seven partitions. Visually, there is an increase in both intensities form the center to the lower and upper vertical regions from part 1 to part 5. In addition, on the region of part 6 and part 7, the plasma starts to terminate. Blue arrows indicate that part 6 region starts to decline at 0.5 mm, 1.9 mm, and 4.5 mm from center. Intensity also diminishes starting at part 6 region. The beam profile intensity at lower vertical region, -6 mm from the center, shows minimal differences. On the contrary, it is observed that the profile at the higher vertical region, 6 mm from the center, shows a wider change in intensity. The decline in intensity is much observable on the upper vertical, from midpoint, regions and starts at in part 6 and part 7. Region on part 7 shows sharp decline in intensity that slightly follows the shape of the target holder.
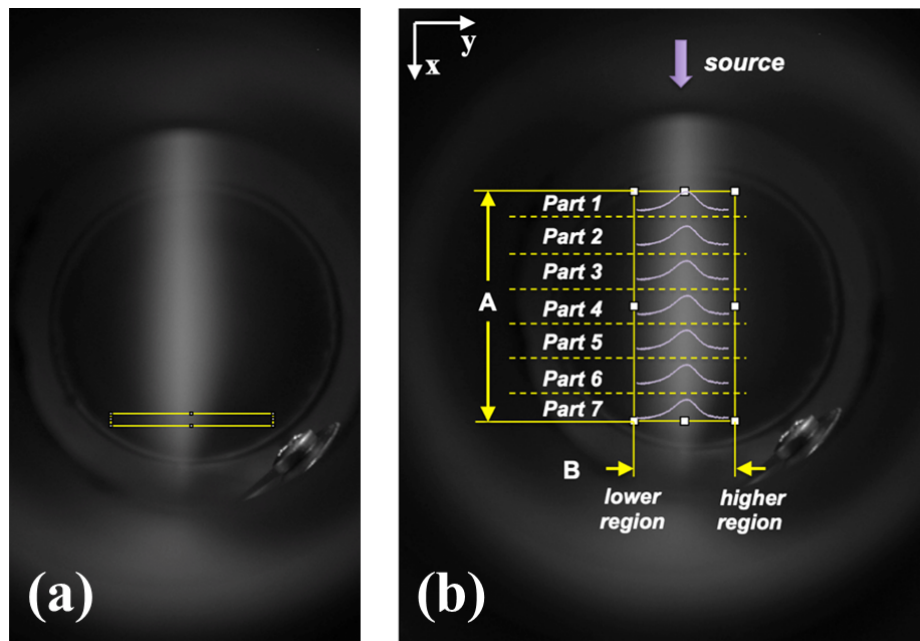
Figure 6.16– Luminous profile intensity at -600 V target bias voltage mapping (spatial

dependence). (a) region of interest and (b) profile mapping partitioning

In addition, Figure 6.16 is retained for all parts of the partition wherein the lower region indicates the lower vertical y-axis of the plasma region while the higher region indicates the upper vertical y-axis of the plasma region. The range between lower and higher region is spatially calibrated with mm unit measurement to approximate the regions wherein the plasma starts to terminate. Visually, the plasma termination approximately follows the angle of inclination of the target holder. Plasma sheath is much thicker at this region.

Varying Target Bias Voltage (V) VS Varying coil current (A). Secondary Extraction Voltage: -10V. Electromagnetic Coil Current: 0A, 5A, 10A, and 15A. On varying coil current: plasma column is thicker at 5A. On increasing target bias. Starting at -300V and -

400V, plasma column shows a slanted feature relative to the target. Sheath on the target surface is thicker.
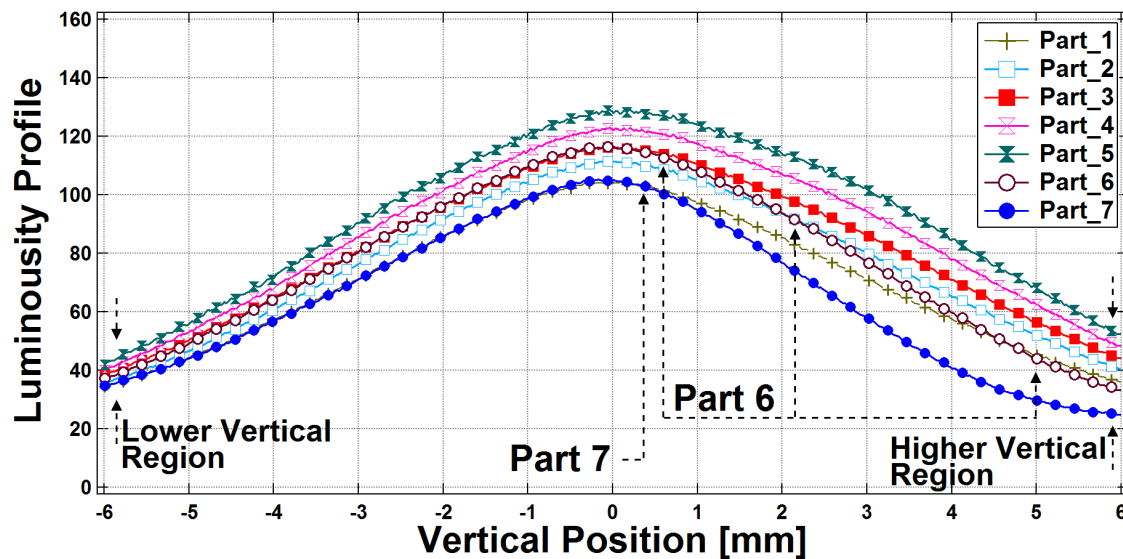
Figure 6.17– Luminosity profile mapping

Figure 6.17 shows that part 6 to 7 shows decline on the higher region of the plasma beam closer to the target compared to the lower region. Nevertheless, lower region is still seen to be affected.

6.4 Hα Doppler Broadening Comparison

The tungsten target was placed at the spectroscopic measurement position and biased at -100 V with respect to the plasma formed in the downstream chamber and the plasma was excited with $I_{D1} = 1.0$ A and $B = 280$ G with the secondary extraction voltage maintained at -10 V and hydrogen pressure at 0.2 Pa. A substantial reduction of the line

broadening at the skirt part of the Hα spectrum has been achieved as shown in Figure 6.18that compares the Hα spectral shapes obtained with both plasma cathodes. The monochromator resolution calibrated by a 1 mm radius hydrogen gas discharge lamp was 23 pm while the spectrum was taken with the duoplasmatron cathode plasma still exhibits 35 pm full width at the half maximum. This reduced spectrum width from 60 pm for the plasma excited by the previous system enabled the observation of the Doppler broadening at the skirt part of the measured Hα spectrum as indicated in Figure 6.18.
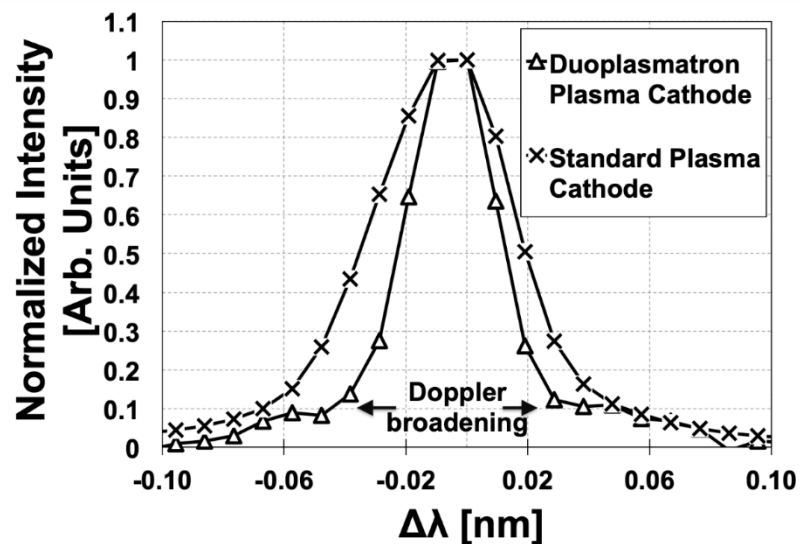
Figure 6.18– Comparison of the particle reflection between the duoplasmatron plasma cathode device (new ion source device) and standard high-temperature DC cathode source (old ion source device) at -100 V target bias voltage. [I_{D1}: 1 A, V_{D1}: 110 V, and I_{coil}: 15 A]

The spectrum shown in Figure 6.18 exhibits an asymmetric broadening with the blue wing shorter than the red wing. Assuming 75 pm as the end of the blue wing, the corresponding hydrogen atom energy is to be 12 eV. In the previous system, spectrum analysis at this low energy range was impossible due to a severe broadening of the tail part.

The operation of the duoplasmatron cathode reduces the hydrogen gas pressure in the measurement region, which should reduce hydrogen ion charge exchange reaction leading to the formation of high-energy atoms to emit photons of Balmer-α wavelength. The contribution from the surface area on the target reflecting incoming ions is one to two orders of magnitude smaller than that from the plasma created by the duoplasmatron source. This smaller area of fast hydrogen atom emission can result in sharper velocity (energy and angular) distribution of atomic hydrogen along the observation axis of the spectrometer. A comparison between the observed spectrum and the velocity distribution obtained by computer simulation (Yamamura, 1983) is being made to see the effect of the target area.

Direct comparisons of the Hα wavelength spectra with the previous plasma cathode discharge were attempted for higher bias voltages. The small diameter of the plasma column created by the duoplasmatron cathode showed a sensitive response to the negative bias applied to the tungsten target.

6.5 Plasma extinction at a higher bias voltage

Figure 6.19 shows the plasma glow when the target was negatively biased at -600 V. The figure clearly shows that the produced plasma does not reach the target, while the diameter appears far larger than the one shown in Figure 6.19 for the case that the target is withdrawn. As the target surface intersects the axis of the plasma guided by the linear magnetic field forming a 45-degree angle, the produced electric field across the sheath seemed to cause a plasma instability near the target. A precise study on the frequency and the density spatial distribution is still under way, but the plasma luminous intensity measurements like Fig. 6.19 clearly show the extinction of plasma glow near the target at

a higher voltage target bias. A duoplasmatron source was originally developed as a high current density positive ion source with the extractable ion current so high that the reduction of the local ion density was necessary to form an ion beam from the plasma passing through the extraction hole (Collins, 1962). The present extraction spacing is far much smaller than the original designs and may not be appropriate for ion extraction. We tried to apply a positive bias to the source for testing if the ion current can be extracted from the plasma source, as previously shown.

Figure 6.19– Duoplasmatron plasma cathode device with plasma termination is observed at -600 V target bias voltage applied to the target. [I_{D1}: 1 A, V_{D1}: 110 V, I_{coil}: 7.5 A, V_{SPS}: -10 V].

Thicker plasmas are often observed at low target voltages, Figure 6.20. The plasma touches down to the target with the radius slightly increased toward the target, which can be explainable as one takes the contribution of secondary electron emission from the target surface into account. Electrons produced at the target surface are accelerated across the sheath having 45-degree angle with respect to the magnetic field lines of force.
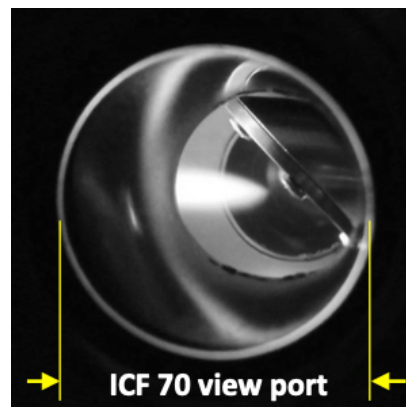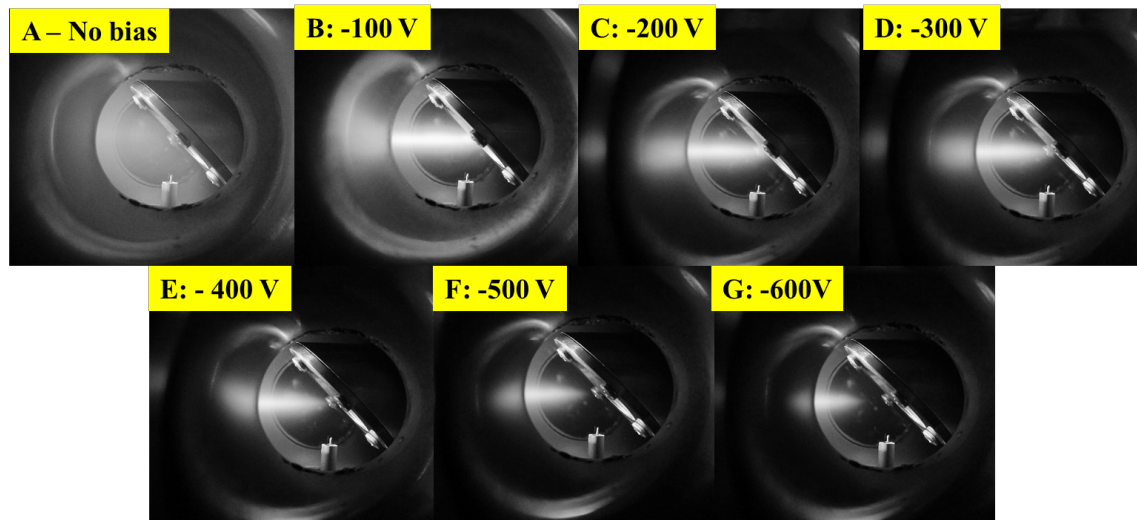
Figure 6.20– Duoplasmatron plasma cathode device with plasma termination at increasing target bias -600 V target bias voltage applied to the target. [I_{D1}: 1 A, V_{D1}: 110 V, I_{coil}: 7.5 A, V_{SPS}: -10 V].

Their kinetic energy is large enough to ionize hydrogen atoms and molecules and the target serves as the second cathode for the case of -100 V target bias. Meanwhile, the plasma radius decreased toward the target biased at -600 V in Fig. 6.20. Positive ions from the plasma may strike the target surface, but they are not guided by magnetized plasma column like the case of -100 V target voltage. Because of the complicated electric field geometry around the target, electrons produced at the target surface has a little possibility to be frozen in magnetic field lines connected to the plasma column. Thus, the secondary electron emission process does not create an ionizing electron source at the tungsten target surface.

6.6   Plasma Instability

The thinning radius plasma column observed in Figure 6.21 seems to suggest an enhanced diffusion caused by a drift instability. A simplified model gives the angular frequency based on an electron density gradient,

$$\omega_D = \frac{v_D}{r_L} = \frac{k_B T}{e n r_L B} \frac{\partial n}{\partial r}$$

where k_B is the Bolzmann constant, T is the electron temperature, n is the electron density, and e is the unit charge of an electron. The frequency is usually very low from several kHz to several 100 kHz. The excitation of large amplitude fluctuation due to drift can be the reason for observing plasma thinning in front of the biased target. The model is shown in Figure 6.22 for the correlation between plasma oscillation target bias schematic diagram to indicate the plasma instability drift concept.
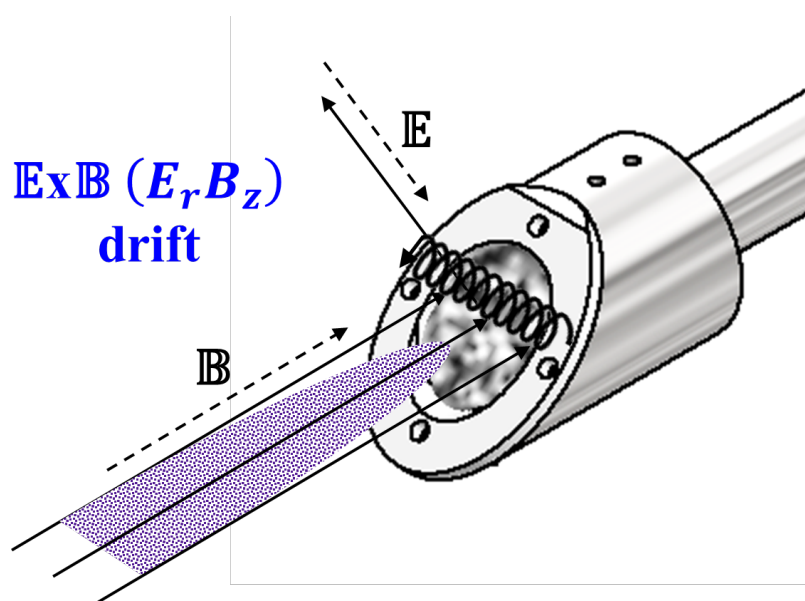
Figure 6.21– Correlation between plasma oscillation target bias schematic diagram

The floating potential of the plasma near the biased target was measured by inserting a Langmuir probe at the position xx cm from the axis of the plasma. The diameter and the length of the tungsten probe electrode tip. Figure 6.22 shows a typical example trace taken by an oscilloscope. The trace clearly indicates a fluctuation with both high and low frequency components.
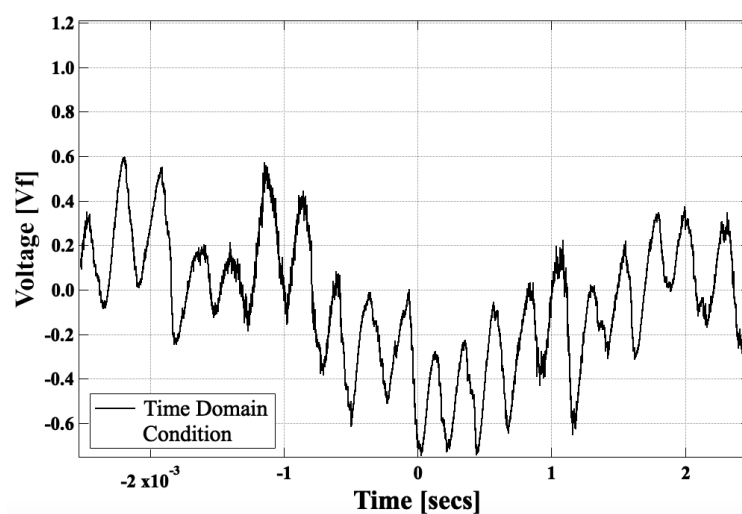
Figure 6.22– Time Domain for low frequency oscillation observed.

The corresponding frequency spectrum shows some low amplitude high frequency components exist above 50 kHz, but the measurements were made to elucidate the change in both amplitude and frequency of the low frequency component below 5 kHz frequency. The frequency spectra for different target bias voltage while keeping the coil current at 7.5 A are shown in Fig. 6.23. As the plasma column starts to destabilize, large amplitude oscillations in the low frequency region are observed. In the present system. The fundamental mode appears around 3 kHz.
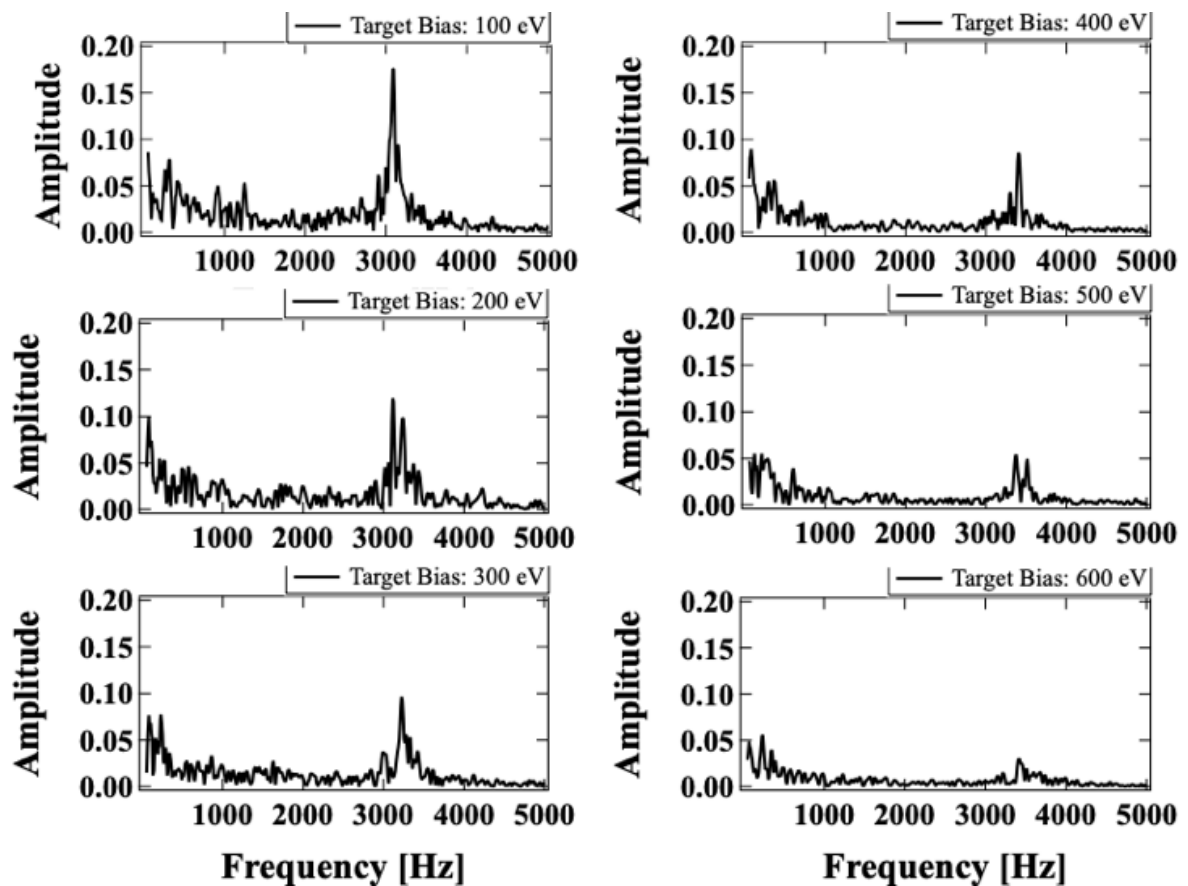
Figure 6.23– Peak Amplitudes at 7.5 A coil current (far from target) at different bias target voltages.

Figure 6.23 shows the dependence of oscillation amplitude and frequency as the function of the target bias voltage. In the graph, the values at the floating potential about 30 V are also shown. The results shown in the figure indicate that the amplitude decreased, and the frequency increased as the negative bias voltage was increased. The reduction in oscillation amplitude by the increasing target bias can be related to the extinction of the plasma near the target, as we have observed in the luminous intensity distribution study; the plasma density around the probe is so small that the electron current density and the fluctuation reaching the probe should be small. On the other hand, the frequency tends to

increase with the increasing bias voltage up to -400 V, while at -500 V and -600 V, the frequency seems saturated around 3.4 kHz.
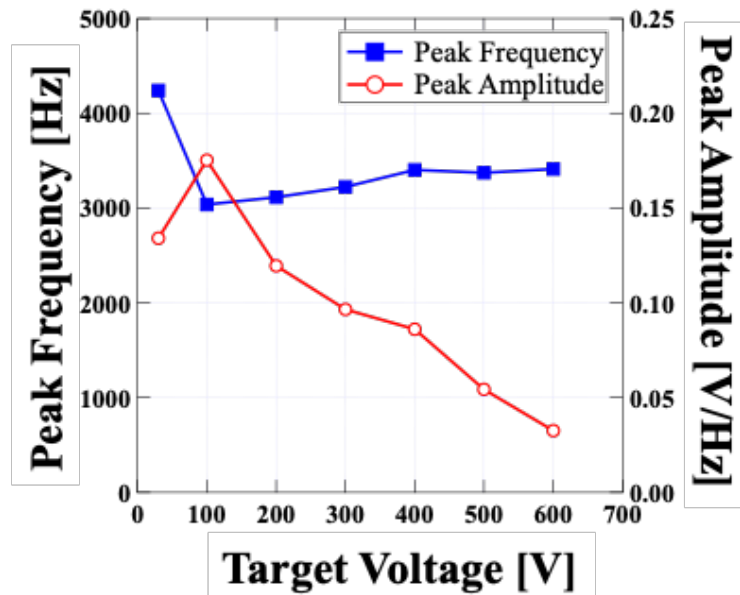
Figure 6.24– Peak Freq. vs Target Bias Voltage and Peak Amp. Vs. Target Bias Voltage

[I_{coil}: 7.5 A, 0.2 Pa Hydrogen Pressure, -10 V sec. extraction current]

As one may see in the original frequency spectrum shown in Figure 6.24, the spectrum intensity had decreased in the entire frequency region, and the probe could be detecting the oscillation of the plasma at a place distant from the probe electrode tip. The increasing frequency characteristics observed from -100 to -400 V can be attributable to a larger density gradient $\frac{\partial n}{\partial r}$ as the consequence of strong electric field in radial direction excited by the target surface having the 45-degree angle with respect to the magnetic field. This model is shown in Figure 6.25– Over-all plasma column size reduction diagram.

As one may see in the original frequency spectrum shown in the previous images, the spectrum intensity had decreased in the entire frequency region, and the probe could be detecting the oscillation of the plasma at a place distant from the probe electrode tip.
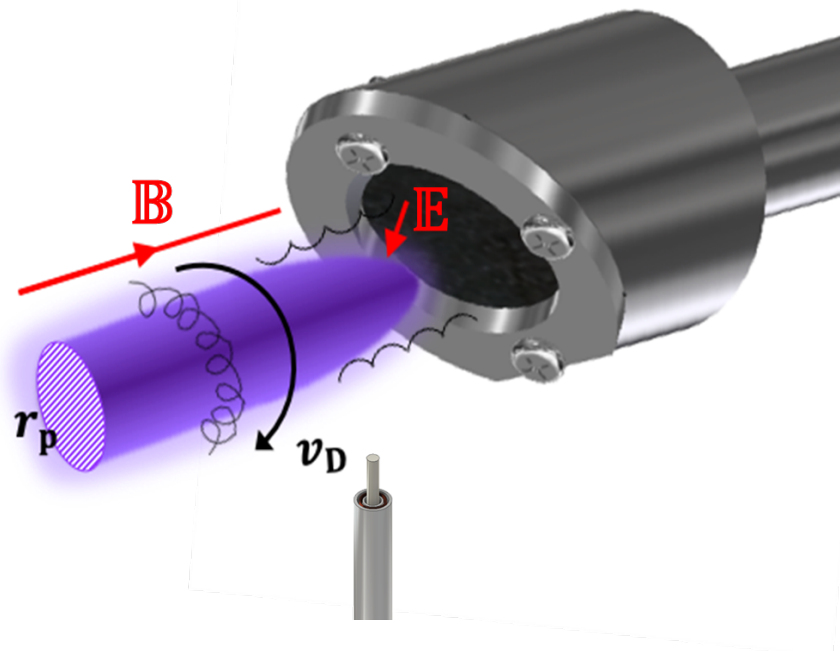
Figure 6.25– Over-all plasma column size reduction diagram.

Chapter Summary

Duoplasmatron ion source is assembled to be a plasma source to provide a thinner beam with the characteristics as a homogeneous plasma cathode source. Extraction geometry must be modified if the present source will serve as a positive ion source. The luminosity profiles realize a very thin plasma. A sharper distribution without any shift from the center while spatial inhomogeneity was observed with the thicker plasma

The Hα wavelength spectrum shows substantial reduction of the line broadening at the skirt part of the $H\alpha$ spectrum has been achieved. The asymmetric broadening with the blue wing (75 pm at the end corresponding to the hydrogen atom energy to be 12 eV) shorter than the red wing.

Plasma instability was encountered, and low frequency oscillations and an enhanced plasma loss were observed. The traces clearly indicate a fluctuation with both high and low frequency components. Observed thinning plasma column length seems to suggest an enhanced diffusion caused by a drift instability and that the plasma column starts to destabilize, large amplitude oscillations in the low frequency region are observed.

References

Collins, L., & Brooker, R. (1962). Ion beam control in a duoplasmatron source. *Nuclear Instruments and Methods, 15*(2), 193-196. doi:10.1016/0029-554x(62)90071-x

Doi, K., Lee, H. T., Tanaka, N., Yamaoka, H., Ueda, Y., & Wada, M. (2018). Spectroscopic study of hydrogen reflection at modified tungsten surface. *Fusion Engineering and Design, 136*, 100-105. doi:10.1016/j.fusengdes.2018.01.001

Doi, K., Yamaoka, H., Kenmotsu, T., & Wada, M. (2018). Spectroscopy Study of Hydrogen Atoms Reflected From Tungsten Surface in a Magnetized Plasma. *IEEE Transactions on Plasma Science, 46*(3), 482-488. doi:10.1109/tps.2018.2803753

Goebel, D., Campbell, G., & Conn, R. (1984). Plasma surface interaction experimental facility (PISCES) for materials and edge physics studies. *Journal of Nuclear Materials, 121*, 277-282. doi:10.1016/0022-3115(84)90135-1

Janev, R. K. (1987). *Elementary processes in hydrogen-helium plasmas: Cross sections and reaction rate coefficients*. Berlin, Heidelberg: Springer-Verlag. doi:10.1007/978-3-642-71935-6

Kuzumi, T., & Wada, M. (2020). Development of a miniaturized duoplasmatron ion source. *Review of Scientific Instruments, 91*(1), 013505. doi:10.1063/1.5128752

Moak, C. D., Banta, H. E., Thurston, J. N., Johnson, J. W., & King, R. F. (1959). Duo

    Plasmatron Ion Source for Use in Accelerators. *Review of Scientific Instruments,*

    30(8), 694-699. doi:10.1063/1.1716726

Plamondon, R., Teichmann, J., & Torven, S. (1988). Current limitation and formation of

    plasma double layers in a non-uniform magnetic field. *Journal of Physics D:*

    Applied Physics, 21(2), 286-292. doi:10.1088/0022-3727/21/2/008

Steenbergen, A. V. (1965). Recent Developments in High Intensity Ion Beam Production

    and Preacceleration. *IEEE Transactions on Nuclear Science, 12*(3), 746-764.

    doi:10.1109/tns.1965.4323729

Takeuchi, H., Yogo, Y., Hattori, T., Tajima, T., & Ishikawa, T. (2017). High-temperature

    Magnetization Characteristics of Steels. *ISIJ International, 57*(10), 1883-1886.

    doi:10.2355/isijinternational.isijint-2017-145

Takeuchi, W., & Yamamura, Y. (1983). Computer studies of the energy spectra and

    reflection coefficients of light ions. *Radiation Effects, 71*(1-2), 53-64.

    doi:10.1080/00337578308218603

Ye, M. (1997). Study of hot tungsten emissive plate in high heat flux plasma on

    NAGDIS-I. *Journal of Nuclear Materials, 241-243*(1), 1243-1247.

    doi:10.1016/s0022-3115(96)00707-6

Chapter 7   Summary and List of Achievements

The Spectroscopic Studies of Excited Species Reflected from Solid Surfaces Irradiated by DC Plasma Cathode Systems were performed. The hydrogen and helium particle reflection on metal targets were observed.

On Doppler broadening of hydrogen on metal surfaces: With the case of tantalum and tungsten, no substantial difference in reflected particle component was observed, while the hint was observed that the material can affect the local concentration of excited molecules near the sample metals. The endpoint and modified clamp effect on the hydrogen reflection mechanism for both tungsten and palladium were discussed. Reflection characteristics were recognizable under a floating potential and at increased bias voltages applied to metal targets under endpoint and modified clamp. Blue and red wings on the spectra were also observed to be balanced on both metal targets under both manifold holders. Hydrogen reflection and ion velocity distributions on the tungsten surface have minimal difference when using either an endpoint or modified clamp. This phenomenon was observed at different bias voltages also. It is suggested that better cooling was present through direct contact of the metal substrate on the substrate holder. This mechanism may provide less adsorbed hydrogen molecules and have higher Doppler-broadening distribution of emission spectra relative to using an endpoint clamp.

Meanwhile, hydrogen velocity distributions for palladium surface showed a difference between emission spectrum for both manifolds. Modified clamp provided higher velocity distributions relative to the endpoint clamp at different bias voltages. It is

suggested that better cooling was present through direct contact of the metal substrate on the substrate holder.

1. **Succeeded in measuring the minute difference between the hydrogen Doppler broadening spectrum between tungsten and palladium metal surface**

2. **Detected the impact on temperature difference by using a modified clamp**

3. **Succeeded in measuring the helium species for triplet states**

On investigation of molecular species in hydrogen plasma near palladium and tungsten surfaces: Hydrogen plasma-metal surface interactions accompany molecular excitations and de-excitations associated with particle reflection at the surfaces. Optical light emissions from molecular species of the hydrogen Fulcher-α ($d^3\Pi_u^- \rightarrow a^3\Sigma_g^+$) Q-Branch at near metal surface region of palladium and tungsten metals were investigated. A wide wavelength range spectrometer indicated a higher emission spectrum of hydrogen plasma on the surface of palladium than tungsten. Meanwhile a high-resolution spectrometer showed the distinct rovibronic lines of the Fulcher-α for electronic levels $v = v' = 0 - 4$ transitions. Rotational temperature, T_{rot}, were computed from the emission spectra lines of hydrogen from palladium and tungsten surfaces. The obtained temperature, T_{rot} for both metal targets showed increase at increasing negative bias voltages applied onto the target of these materials. Hydrogen plasma on palladium surface indicated higher molecular excitations than that on the tungsten surface. Optical emission spectroscopy showed trend in the Balmer-γ, Balmer-β, Fulcher- α and Balmer-α region of palladium producing higher excitation in atoms and molecules in the plasma region than tungsten metal sheets. Rotational temperature T_{rot} determination from the observed intensities of

rovibronic lines indicated that palladium interaction with hydrogen plasma produced higher densities of excited molecules than tungsten.

4. **Confirm the gas heating effect was not responsible for the Balmer alpha broadening through molecular spectroscopic measurement**

On plasma excitation in a dc linear magnetic field by a duoplasmatron plasma cathode: A compact duoplasmatron source was designed and used as the plasma cathode for exciting plasma in a linear magnetic field. A plasma column with a sharp boundary has been successfully produced, and the improvement in the accuracy of Doppler broadening measurement was realized. By collecting more information on broadening by observing pressure dependence and plasma size dependence, the reason for observing unexpected broadening at the skirt part of the Hα line spectrum is expected to be clarified. The formed narrow ionizing electron channel is found sensitive to the local electric field near the target, and the preparation of a target with the surface intersecting the magnetic field perpendicularly can stabilize the plasma transport down to the target surface. The designed source also has the potential to serve as a hydrogen positive ion source that delivers ion current to the target. Plasma instability was investigated and presented to exist at higher target bias voltage.

5. **Tested the duoplasmatron plasma source to resize the plasma shape and succeeded in narrowing the central Doppler broadening width**